

Central Lancashire Online Knowledge (CLoK)

Title	The JCMT BISTRO Survey: Unveiling the Magnetic Fields around Galactic Center
Type	Article
URL	https://clock.uclan.ac.uk/55259/
DOI	https://doi.org/10.3847/1538-4357/adbe34
Date	2025
Citation	Yang, Meng-Zhe, Lai, Shih-Ping, Karoly, Janik, Pattle, Kate, Lu, Xing, Eden, David, Lin, Sheng-Jun, Poidevin, Frédérick, Sharma, Ekta et al (2025) The JCMT BISTRO Survey: Unveiling the Magnetic Fields around Galactic Center. <i>The Astrophysical Journal</i> , 983 (2). ISSN 0004-637X
Creators	Yang, Meng-Zhe, Lai, Shih-Ping, Karoly, Janik, Pattle, Kate, Lu, Xing, Eden, David, Lin, Sheng-Jun, Poidevin, Frédérick, Sharma, Ekta, Hwang, Jihye, Fanciullo, Lapo, Tahani, Mehrnoosh, Koch, Patrick M., Inutsuka, Shu-ichiro, Le Gouellec, Valentin J. M., Duan, Hao-Yuan, Wang, Jia-Wei, Fuller, Gary, Furuya, Ray S., Gu, Qilao, Hasegawa, Tetsuo, Li, Guangxing, Liu, Junhao, Akshaya, M. S., Najimudeen, Bijas, Tram, Le Ngoc, Ward-Thompson, Derek, Arzoumanian, Doris, Di Francesco, James, Doi, Yasuo, Hoang, Thiem, Kang, Ji-hyun, Kwon, Jungmi, Kwon, Woojin, Lee, Chang Won, Liu, Tie, Onaka, Takashi, Sadavoy, Sarah, Tamura, Motohide, Bastien, Pierre, Berry, David, Coudé, Simon and Qiu, Keping

It is advisable to refer to the publisher's version if you intend to cite from the work.
<https://doi.org/10.3847/1538-4357/adbe34>

For information about Research at UCLan please go to <http://www.uclan.ac.uk/research/>

All outputs in CLoK are protected by Intellectual Property Rights law, including Copyright law. Copyright, IPR and Moral Rights for the works on this site are retained by the individual authors and/or other copyright owners. Terms and conditions for use of this material are defined in the <http://clock.uclan.ac.uk/policies/>

Central Lancashire Online Knowledge (CLoK)

Title	The JCMT BISTRO Survey: Unveiling the Magnetic Fields around Galactic Center
Type	Article
URL	https://clock.uclan.ac.uk/55259/
DOI	https://doi.org/10.3847/1538-4357/adbe34
Date	2025
Citation	Yang, Meng-Zhe, Lai, Shih-Ping, Karoly, Janik, Pattle, Kate, Lu, Xing, Eden, David, Lin, Sheng-Jun, Poidevin, Frédérick, Sharma, Ekta et al (2025) The JCMT BISTRO Survey: Unveiling the Magnetic Fields around Galactic Center. <i>The Astrophysical Journal</i> , 983 (2). ISSN 1538-4357
Creators	Yang, Meng-Zhe, Lai, Shih-Ping, Karoly, Janik, Pattle, Kate, Lu, Xing, Eden, David, Lin, Sheng-Jun, Poidevin, Frédérick, Sharma, Ekta, Hwang, Jihye, Fanciullo, Lapo, Tahani, Mehrnoosh, Koch, Patrick M., Inutsuka, Shu-ichiro, Le Gouellec, Valentin J. M., Duan, Hao-Yuan, Wang, Jia-Wei, Fuller, Gary, Furuya, Ray S., Gu, Qilao, Hasegawa, Tetsuo, Li, Guangxing, Liu, Junhao, Akshaya, M. S., Najimudeen, Bijas, Tram, Le Ngoc, Ward-Thompson, Derek, Arzoumanian, Doris, Di Francesco, James, Doi, Yasuo, Hoang, Thiem, Kang, Ji-hyun, Kwon, Jungmi, Kwon, Woojin, Lee, Chang Won, Liu, Tie, Onaka, Takashi, Sadavoy, Sarah, Tamura, Motohide, Bastien, Pierre, Berry, David, Coudé, Simon and Qiu, Keping

It is advisable to refer to the publisher's version if you intend to cite from the work.
<https://doi.org/10.3847/1538-4357/adbe34>

For information about Research at UCLan please go to <http://www.uclan.ac.uk/research/>

All outputs in CLoK are protected by Intellectual Property Rights law, including Copyright law. Copyright, IPR and Moral Rights for the works on this site are retained by the individual authors and/or other copyright owners. Terms and conditions for use of this material are defined in the <http://clock.uclan.ac.uk/policies/>



The JCMT BISTRO Survey: Unveiling the Magnetic Fields around Galactic Center

Meng-Zhe Yang¹, Shih-Ping Lai^{1,2}, Janik Karoly³, Kate Pattle³, Xing Lu (吕行)⁴, David Eden^{5,6}, Sheng-Jun Lin²,
 Frédéric Poidevin^{7,8}, Ekta Sharma⁹, Jihye Hwang¹⁰, Lapo Fanciullo¹¹, Mehrmoosh Tahani¹², Patrick M. Koch²,
 Shu-ichiro Inutsuka¹³, Valentin J. M. Le Gouellec^{14,15}, Hao-Yuan Duan^{1,16}, Jia-Wei Wang², Gary Fuller¹⁷,
 Ray S. Furuya¹⁸, Qilao Gu⁴, Tetsuo Hasegawa (長谷川哲夫)¹⁹, Guangxing Li²⁰, Junhao Liu (劉峻豪)²¹,
 M. S. Akshaya¹⁰, Bijas Najimudeen¹⁷, Le Ngoc Tram²², Derek Ward-Thompson²³, Doris Arzoumanian²⁴,
 James Di Francesco^{25,26}, Yasuo Doi²⁷, Thiem Hoang¹⁰, Ji-hyun Kang¹⁰, Jungmi Kwon²⁸, Woojin Kwon^{29,30,31},
 Chang Won Lee (이창원)^{10,32}, Tie Liu (劉鐵)³³, Takashi Onaka³⁴, Sarah Sadavoy³⁵, Motohide Tamura^{19,34},
 Pierre Bastien³⁶, David Berry³⁷, Simon Coude³⁸, and Keping Qiu^{39,40}

¹ Institute of Astronomy and Department of Physics, National Tsing Hua University, Hsinchu 30013, Taiwan; jeremys93102@gapp.nthu.edu.tw

² Academia Sinica Institute of Astronomy and Astrophysics, No.1, Sec. 4., Roosevelt Road, Taipei 10617, Taiwan

³ Department of Physics and Astronomy, University College London, WC1E 6BT London, UK

⁴ Shanghai Astronomical Observatory, Chinese Academy of Sciences, 80 Nandan Road, Shanghai 200030, People's Republic of China

⁵ Department of Physics, University of Bath, Claverton Down, Bath BA2 7AY, UK

⁶ Armagh Observatory and Planetarium, College Hill, Armagh BT61 9DB, UK

⁷ Instituto de Astrofísica de Canarias, Vía Láctea, 38205 La Laguna, Tenerife, Spain

⁸ Universidad de La Laguna, Departamento de Astrofísica, 38206 La Laguna, Tenerife, Spain

⁹ CAS Key Laboratory of FAST, National Astronomical Observatories, Chinese Academy of Sciences, People's Republic of China

¹⁰ Korea Astronomy and Space Science Institute, 776 Daedeokdae-ro, Yuseong-gu, Daejeon 34055, Republic of Korea

¹¹ National Chung Hsing University, 145 Xingda Rd., South Dist., Taichung City 402, Taiwan

¹² Banting and KIPAC Fellow: Kavli Institute for Particle Astrophysics and Cosmology (KIPAC), Stanford University, Stanford, CA, USA

¹³ Department of Physics, Graduate School of Science, Nagoya University, Furo-cho, Chikusa-ku, Nagoya 464-8602, Japan

¹⁴ Institut de Ciències de l'Espai (ICE-CSIC), Campus UAB, Can Magrans S/N, E-08193 Cerdanyola del Vallès, Catalonia, Spain

¹⁵ Institut d'Estudis Espacials de Catalunya (IEEC), Campus del Baix Llobregat - UPC, Esteve Terradas 1, E-08860 Castelldefels, Catalonia, Spain

¹⁶ Taipei Astronomical Museum, Taipei, Taiwan

¹⁷ Jodrell Bank Centre for Astrophysics, School of Physics and Astronomy, University of Manchester, Oxford Road, Manchester, M13 9PL, UK

¹⁸ Institute of Liberal Arts and Sciences Tokushima University, Minami Jousanajima-machi 1-1, Tokushima 770-8502, Japan

¹⁹ National Astronomical Observatory of Japan, National Institutes of Natural Sciences, Osawa, Mitaka, Tokyo 181-8588, Japan

²⁰ Yunnan University, People's Republic of China

²¹ Division of ALMA, National Astronomical Observatory of Japan, Mitaka, Tokyo 181-8588, Japan

²² University of Science and Technology of Hanoi, Vietnam Academy of Science and Technology, 18 Hoang Quoc Viet, Hanoi, Vietnam

²³ Jeremiah Horrocks Institute, University of Central Lancashire, Preston PR1 2HE, UK

²⁴ Division of Science, National Astronomical Observatory of Japan, 2-21-1 Osawa, Mitaka, Tokyo 181-8588, Japan

²⁵ NRC Herzberg Astronomy and Astrophysics, 5071 West Saanich Road, Victoria, BC V9E 2E7, Canada

²⁶ Department of Physics and Astronomy, University of Victoria, Victoria, BC V8W 2Y2, Canada

²⁷ Department of Earth Science and Astronomy, Graduate School of Arts and Sciences, The University of Tokyo, 3-8-1 Komaba, Meguro, Tokyo 153-8902, Japan

²⁸ Department of Astronomy, University of Tokyo, 7-3-1 Hongo, Bunkyo-ku, Tokyo 113-0033, Japan

²⁹ Department of Earth Science Education, Seoul National University, 1 Gwanak-ro, Gwanak-gu, Seoul 08826, Republic of Korea

³⁰ SNU Astronomy Research Center, Seoul National University, 1 Gwanak-ro, Gwanak-gu, Seoul 08826, Republic of Korea

³¹ The Center for Educational Research, Seoul National University, 1 Gwanak-ro, Gwanak-gu, Seoul 08826, Republic of Korea

³² University of Science and Technology, Korea (UST), 217 Gajeong-ro, Yuseong-gu, Daejeon 34113, Republic of Korea

³³ Key Laboratory for Research in Galaxies and Cosmology, Shanghai Astronomical Observatory, Chinese Academy of Sciences, 80 Nandan Road, Shanghai 200030, People's Republic of China

³⁴ Department of Astronomy, Graduate School of Science, The University of Tokyo, 7-3-1 Hongo, Bunkyo-ku, Tokyo 113-0033, Japan

³⁵ Department for Physics, Engineering Physics and Astrophysics, Queen's University, Kingston, ON, K7L 3N6, Canada

³⁶ Centre de recherche en astrophysique du Québec & département de physique, Université de Montréal, C.P. 6128 Succ. Centre-ville, Montréal, QC, H3C 3J7, Canada

³⁷ East Asian Observatory, 660 N. A'ohōkū Place, University Park, Hilo, HI 96720, USA

³⁸ SOFIA Science Center, Universities Space Research Association, NASA Ames Research Center, Moffett Field, CA 94035, USA

³⁹ School of Astronomy and Space Science, Nanjing University, 163 Xianlin Avenue, Nanjing 210023, People's Republic of China

⁴⁰ Key Laboratory of Modern Astronomy and Astrophysics (Nanjing University), Ministry of Education, Nanjing 210023, People's Republic of China

Received 2024 October 22; revised 2025 March 4; accepted 2025 March 5; published 2025 April 18

Abstract

We acquired 450 and 850 μm dust continuum polarization observations toward the inner region of the Central Molecular Zone (CMZ) as part of the *B*-Fields In Star-forming Region Observations survey using the POL-2 polarimeter on the James Clerk Maxwell Telescope. These observations encompassed three dense structures: the 20 km s⁻¹ cloud (20MC), 50 km s⁻¹ cloud (50MC), and circumnuclear disk (CND). Our aim is to investigate the magnetic field morphology and strength in the inner region of the CMZ using polarized dust continuum and the Davis–Chandrasekhar–Fermi method. The magnetic field morphology is highly ordered in all three dense regions. The plane-of-sky magnetic field strengths are ~ 1 mG for the 20MC and the 50MC, and ~ 2 mG for the CND. We

compare the energy contributions of turbulence, gravity, and thermal motion with that of the magnetic field using the plasma β , mass-to-flux ratio, and Alfvén Mach number. The outcomes reveal the magnetic field stands out as the predominant factor within the inner region of the CMZ. The dominance of the magnetic field may explain the low star-forming rate in the CMZ. We further investigate the dust grain alignment efficiency by exploring the relationship between polarization fraction and total intensity. The results suggest that dust grains are well aligned with the magnetic fields.

Unified Astronomy Thesaurus concepts: [Interstellar medium \(847\)](#); [Star forming regions \(1565\)](#); [Magnetic fields \(994\)](#); [Galactic center \(565\)](#); [Submillimeter astronomy \(1647\)](#)

1. Introduction

The Central Molecular Zone (CMZ), the inner region of the Milky Way with a radius of ~ 200 pc (M. Morris & E. Serabyn 1996), contains over $10^7 M_{\odot}$ of molecular gas (K. Ferrière et al. 2007; X. Lu et al. 2017b). The molecular clouds within the CMZ are warmer and more turbulent compared to those in the Galactic disk (M. Tsuboi & A. Miyazaki 2012). The star formation rate (SFR) is typically proportional to the gas surface density or the gas volume density (M. Schmidt 1959; R. C. Kennicutt 1998; R. C. Kennicutt & N. J. Evans 2012). The typical SFR in the CMZ, however, is approximately 10 times lower than that in other regions of the Milky Way (S. N. Longmore et al. 2013; J. M. D. Kruijssen et al. 2014).

X. Lu et al. (2019) investigated the SFR in six massive CMZ clouds, including the 20 km s^{-1} cloud, the 50 km s^{-1} cloud, G.0253+0.016 (the Brick), Sgr B1-off, and Sgr C, using observations from the Submillimeter Array (SMA) and Very Large Array (VLA), also utilizing data from A. Ginsburg et al. (2018) for Sgr B2. Among these regions, Sgr B2 and Sgr C follow the dense gas star formation relation inferred from nearby clouds; however, the SFRs in the other four clouds are approximately 1 order of magnitude lower. X. Lu et al. (2019) suggested that the low SFR is attributed to the presence of strong turbulence, resulting in a significantly lower amount of gas confined in gravitationally bound cores, indicating a magnetically supercritical environment. Apart from these massive molecular clouds, in the region close to Sgr A*, turbulence dominates the internal energy and suppresses star formation at distances greater than 1 pc. Meanwhile, tidal forces dominate within 1 pc, as suggested by the unmagnetized virial theorem (P.-Y. Hsieh et al. 2021).

In general, the initiation of the star-forming process occurs within magnetized and turbulent molecular clouds. The magnetic field can play multiple roles, inhibiting gravitational collapse, reducing star formation efficiency (e.g., F. Nakamura & Z.-Y. Li 2008; J.-W. Wang et al. 2019), and mitigating angular momentum (e.g., L. Mestel 1985; T. C. Mouschovias & E. V. Paleologou 1986). Characterizing the magnetic field within the CMZ is therefore pivotal for understanding the underlying reasons for its relatively low SFR.

The 20 km s^{-1} cloud and 50 km s^{-1} cloud, which are named after their local standard of the rest radial velocities (hereinafter referred to 20MC and 50MC, respectively), are two massive molecular clouds close to Sgr A* with low SFRs, as mentioned above. For the 20MC, X. Lu et al. (2017a) proposed that the star-forming process is still in an early evolutionary phase based on the observable H_2O masers combined with the nondetection of Class II CH_3OH masers and ultracompact H II region. J. M. D. Kruijssen et al. (2015) proposed that star formation within this massive cloud is possibly triggered by tidal compression. In contrast, several compact H II regions have been observed in the 50MC (e.g., F. Yusef-Zadeh et al. 2010; E. Mills et al. 2011). This cloud,

with huge amounts of shocked molecular gas traced by SiO (2–1), was proposed to be a candidate of a massive star-forming region induced by cloud–cloud collision (M. Tsuboi et al. 2015; K. Uehara et al. 2019). Both tidal compression and cloud–cloud collision can lead to severe turbulence, which may play a crucial role during the star-forming process.

In addition to severe turbulence, the magnetic field also appears to be strong in CMZ clouds (e.g., M. Morris & F. Yusef-Zadeh 1989). The magnetic field orientations are highly ordered in this region (e.g., P.-Y. Hsieh et al. 2018; A. Mangilli et al. 2019; Y. Hu et al. 2022). Recently, D. Paré et al. (2024) presented the magnetic field morphology within the CMZ region using SOFIA/HAWC+ observations at $214 \mu\text{m}$. The distribution of polarization pseudovectors reveals a bimodal pattern in the CMZ magnetic field orientations, showing field components that align either parallel or perpendicular to the Galactic plane.

For the active star-forming cloud Sgr B2, R. M. Crutcher (1999) measured a line-of-sight (LOS) magnetic field strength of $480 \mu\text{G}$ using Zeeman measurements and estimated the mass-to-flux ratio to be ~ 2.6 , suggesting the cloud is magnetically supercritical. In comparison, T. Pillai et al. (2015) estimated the plane-of-sky (POS) magnetic field strength within the inactive star-forming cloud G0.253+0.016 using the Davis–Chandrasekhar–Fermi (DCF) method with $850 \mu\text{m}$ polarization observations taken by the James Clerk Maxwell Telescope (JCMT) equipped with the polarimeter SCUPOL. They obtained a POS magnetic field strength of $\sim 5 \text{ mG}$ and estimated the mass-to-flux ratio to be around 0.6, suggesting that the magnetic fields may impede gravitational collapse. These findings suggest the magnetic field may be an important factor in determining the SFR in the CMZ.

The closest molecular gas reservoir near the Galactic center is the circumnuclear disk (CND) of the Milky Way, which is a torus-like structure rotating around Sgr A* with a radius from 2 to 5 pc (e.g., H. M. Latvakoski et al. 1999; M. Tsuboi et al. 2018; P.-Y. Hsieh et al. 2019; D. Paré et al. 2024). The magnetic field strength toward the CND was measured to be $\sim 3 \text{ mG}$, as obtained from Zeeman measurements by R. L. Plante et al. (1995). The magnetic field is dynamically important and influencing the gas motion in CND. It not only supports the gas against gravity but also contributes to accretion toward Sgr A* by removing angular momentum. M. Wardle & A. Konigl (1990) modeled the magnetic field in this region as an accretion disk threaded by open magnetic field lines. The angular momentum is effectively removed when the angle between the poloidal component of the magnetic field (the component in the r - z plane, where r is the radial direction, and z is the symmetry axis relative to a reference torus) and the disk surface is less than $\sim 55^\circ$. R. H. Hildebrand et al. (1990, 1993) measured the polarization of the far-infrared thermal emission in the CND, and showed that the observations were consistent with the model proposed by M. Wardle & A. Konigl (1990).

Table 1
Properties of Continuum Observations

Region	Observed Position ^a		Duration (hr)	$\langle \delta I_{450 \mu\text{m}} \rangle^b$ (Jy beam ⁻¹)	$\langle \delta I_{850 \mu\text{m}} \rangle^b$ (Jy beam ⁻¹)	$\langle \sigma_{QU,450 \mu\text{m}} \rangle^b$ (Jy beam ⁻¹)	$\langle \sigma_{QU,850 \mu\text{m}} \rangle^b$ (Jy beam ⁻¹)
	l (deg)	b (deg)					
M20AL018							
Field 1	359.883033	-0.074825	1.5	8.01	0.04	66.54	3.99
M17AP074							
Field 2	0.042601	-0.010758	4.0	7.51	0.05	85.92	5.94
Field 3	359.944160	-0.046052	7.5	3.51	0.05	52.21	3.89
Field 4	359.884075	-0.071629	4.4	7.80	0.04	59.78	3.94

Notes. The observations from project M20AL018 cover the south region (Field 1); the observations from project M17AP074 cover the north (Field 2), middle (Field 3), and south (Field 4) regions.

^a The observed position is expressed in Galactic coordinates.

^b These values are the rms average of the 4'' mosaic maps within the central 3' regions centered on the observed positions.

In this paper, we present the 450 and 850 μm observations toward the Galactic center taken by the Submillimetre Common-User Bolometer Array 2 (SCUBA-2; W. S. Holland et al. 2013) instrument and its associated polarimeter POL-2 (P. Bastien et al. 2011; P. Friberg et al. 2016) equipped on JCMT. These data were taken as part of the *B*-fields In STar forming Regions Observations (BISTRO) survey (D. Ward-Thompson et al. 2017; J. Kwon et al. 2018; A. Soam et al. 2018; J. Liu et al. 2019). We explore the magnetic field morphology and strengths within the 20MC, 50MC, and CND. Meanwhile, an overview of the survey data and a global analysis of the 850 μm magnetic field across the entire CMZ are presented in J. Karoly et al. (2025).

In star-forming regions, the alignment efficiency of dust grains can be quantified by the power index of the dependence of the polarization fraction on total intensity, $p \propto I^{-\alpha}$ (D. C. B. Whittet et al. 2008). We investigate the power-law relation between polarization fraction and total intensity using the Ricean Mean Model proposed by K. Pattle et al. (2019) to examine whether dust grains are aligned by magnetic fields or not.

The organization of this paper is as follows. In Section 2, we provide a detailed account of the observed data from JCMT BISTRO and outline the ancillary data used in the estimation of magnetic field strength. In Section 3, we determine the magnetic field morphology and strength through the analysis of JCMT BISTRO observations. Using the derived magnetic field strength, we then explore energy contributions from turbulence, gravity, thermal motion, and the magnetic field. Additionally, we assess the alignment efficiency of dust grains. Discussions are presented in Section 4, and we draw conclusions in Section 5.

2. Observations

2.1. JCMT SCUBA-2/POL-2 Observations

The 450 and 850 μm continuum and polarization observations were obtained using SCUBA-2 equipped with the POL-2 polarimeter on the JCMT 15 m telescope (project code: M20AL018, M17AP074). We observed the 20MC, 50MC, and CND using four pointings (see Table 1). The effective beam sizes of the JCMT are 9''.8 at 450 μm and 14''.6 at 850 μm (J. T. Dempsey et al. 2013), corresponding to length scales of ~ 0.39 pc and ~ 0.59 pc, respectively, based on a distance of 8.34 kpc to Sgr A* (M. J. Reid et al. 2014).

We reduced the raw data following a three-stage process using *pol2map* routine, which is contained in the SCUBA-2 map-making software SMURF (D. S. Berry et al. 2005; E. L. Chapin et al. 2013). The POL-2 data reduction was described in detail by J. Hwang et al. (2021). The final mosaicked maps with a pixel size of 4'' are created by coadding the Stokes *I*, *Q*, *U* maps. To achieve better sensitivity, the final debiased polarization catalog is binned to 12''. The produced maps of Stokes *I*, *Q*, *U* have units of pW. To convert the instrumental unit to the physical flux unit of Jy beam⁻¹, we applied the flux conversion factors (FCFs) of 531 for 450 μm and 516 for 850 μm , as recommended by S. Mairs et al. (2021). The FCFs for the observations taken by SCUBA-2 equipped with POL-2 are 1.96 and 1.35 times higher than the ones only taken by SCUBA-2 at 450 and 850 μm , respectively.

We adopt the asymptotic estimator, which was introduced by J. F. C. Wardle & P. P. Kronberg (1974), to calculate the debiased linear polarization fraction p , as follows (*I*, *Q*, and *U* are the Stokes parameters, whose uncertainties are denoted as δI , δQ , and δU , respectively):

$$p = \frac{PI}{I} = \frac{\sqrt{Q^2 + U^2 - \sigma_{QU}^2}}{I}, \quad (1)$$

where the weighted mean variance for *Q* and *U*, σ_{QU}^2 , is

$$\sigma_{QU}^2 = \frac{Q^2 \delta Q^2 + U^2 \delta U^2}{Q^2 + U^2}. \quad (2)$$

Here, PI is the debiased polarization intensity. The σ_{QU} indicates the uncertainty of both the debiased and nonbiased polarization intensity, δPI .

If $(Q^2 + U^2) < \sigma_{QU}^2$, p will be treated as 0. The uncertainty on polarization fraction (both debiased and nonbiased) is defined as

$$\delta p = \frac{\sqrt{Q^2 \delta Q^2 + U^2 \delta U^2 + p^4 I^2 \delta I^2}}{p I^2}. \quad (3)$$

In addition, the polarization position angle (θ_p) and its uncertainty ($\delta \theta_p$) are calculated using the following formulae:

$$\theta_p = \frac{1}{2} \arctan \left(\frac{U}{Q} \right), \quad (4)$$

$$\delta\theta_p = \frac{1}{2} \sqrt{\frac{(Q^2\delta U^2 + U^2\delta Q^2)}{(Q^2 + U^2)^2}}. \quad (5)$$

2.2. JCMT CHIMPS2 Observations

We utilize the ^{12}CO (3–2) data from the CO Heterodyne Inner Milky Way Plane Survey 2 (CHIMPS2), obtained with the Heterodyne Array Receiver Program (HARP) on the JCMT (D. J. Eden et al. 2020), to evaluate the contamination from CO emission. These observations cover the CMZ within the range of $-3^\circ \leq l \leq +5^\circ$ and $-0.5 \leq b \leq +0.5$. The velocity range extends from -250 to 300 km s^{-1} with a resolution of 1 km s^{-1} .

2.3. Contamination of Dust Continuum with CO Emission

The ^{12}CO (6–5) line (691.473 GHz) and ^{12}CO (3–2) line (345.796 GHz) are close to the centers of the continuum bandpass filters at $450 \mu\text{m}$ (664 GHz) and at $850 \mu\text{m}$ (355 GHz), respectively, indicating that the CO spectral line emissions may contaminate the continuum observations. We use the ^{12}CO (3–2) contamination fraction provided by H. Parsons (2017) to correct the Stokes I map at $850 \mu\text{m}$. Then, we infer the potential line contamination from ^{12}CO (6–5) to $450 \mu\text{m}$ continuum observation using ^{12}CO (3–2) contamination fraction under the assumption of a local thermodynamic equilibrium (see E. Drabek et al. 2012). We assume that the CO emission is unpolarized, which does not affect the Stokes Q and U .

Due to missing flux issue, we did not use BISTRO Stokes I and CHIMPS2 data to estimate the CO contamination. We have attempted to remove CO contamination during the reduction process using CHIMPS2 ^{12}CO (3–2) observations. We obtained unreasonable results with negative contamination levels or more than 100%, however, possibly due to the missing flux problem in POL-2. The observing mode used for our BISTRO data is DAISY, which is designed for compact sources of $\sim 3'$ or smaller. The CHIMPS2 observations, which use the PONG observing mode, are not suitable for incorporation into our data. Detailed descriptions and a discussion of the missing flux issue are provided in Appendix. This issue is also apparent in Section 3.2.1, where we use Herschel data to fit the spectral energy distribution (SED).

2.4. Nobeyama Observations

We apply observations of C^{18}O (1–0) using the 45 m telescope at Nobeyama Radio Observatory (NRO) to analyze the velocity dispersion of the nonthermal component of magnetized turbulence. These observations have a resolution of $15''$, similar to the resolutions of our JCMT data. S. Tokuyama et al. (2019) conducted these observations using the FOur-beam REceiver System for the NRO (T. Minamidani et al. 2016) during the period of 2016 January 26–31. The observed region covered the range of approximately $-1.4 \leq l \leq +1.4$ and $-0.35 \leq b \leq +0.35$, using the on-the-fly (OTF) mapping mode. The data were smoothed using a $15''$ Bessel-Gauss function and sampled on a grid of $7.5 \times 7.5 \times 2 \text{ km s}^{-1}$.

2.5. Herschel Hi-GAL

We obtained the image of continuum emissions at 160, 250, 350, and $500 \mu\text{m}$ from the Herschel Infrared Galactic Plane

Survey (Hi-GAL; S. Molinari et al. 2016), a key program of the Herschel satellite (G. L. Pilbratt et al. 2010), to determine the dust temperature and opacity spectral index by fitting the SED. These data are convolved using Gaussian kernels to achieve a common spatial resolution of $36''$ corresponding to that at $500 \mu\text{m}$.

3. Results

3.1. Magnetic Field Morphology

Polarization at submillimeter wavelengths is thought to originate from asymmetric dust grains aligned with magnetic fields (L. Davis & J. L. Greenstein 1951; B. T. Draine & J. C. Weingartner 1996; A. Lazarian & T. Hoang 2007; B. G. Andersson et al. 2015). To infer the magnetic field morphology, we rotate the polarization position angles by 90° (B. G. Andersson et al. 2015).

The question arises of whether we need to be concerned about contamination of our observations by foreground emission. JCMT SCUBA-2/POL-2 data are fundamentally insensitive to extended emission due to the necessity of accounting for atmospheric emission, with any astrophysical signal on size scales comparable to or larger than the SCUBA-2 array size being indistinguishable from the atmospheric signal and thus removed in the data reduction process, leading all SCUBA-2 and POL-2 maps to have a zero background (E. L. Chapin et al. 2013).

The response of SCUBA-2 is thus very strongly weighted toward compact, high-column density structures (e.g., D. Ward-Thompson et al. 2016), and the small map size and slow scanning speed of POL-2 further suppress the recovery of extended emission (P. Friberg et al. 2016). Our expectation that all of our emission arises from the 20MC, 50MC, and CND, rather than from diffuse extended foregrounds, is supported by the analysis of PILOT observations by A. Mangilli et al. (2019), who found a significant discrepancy between PILOT and SCUPOL (the predecessor to POL-2) observations on the position of the 50MC. However, when they performed background subtraction on the PILOT data to mimic the spatial frequencies present in the JCMT SCUPOL data, they found that the two measurements agree well. This further suggests that the structures that we observe in the Galactic center do not have a significant contribution from extended foreground or background emission along the LOS.

3.1.1. B Field Orientations from BISTRO Observations

Figure 1 illustrates the overall magnetic field morphology traced by POL-2 polarization with a pixel size of $12''$ at 450 and $850 \mu\text{m}$, overlaid on the Stokes I map containing CO contamination with a pixel size of $4''$. The polarization half-vectors were selected based on the signal-to-noise ratio (SNR) of Stokes I ($\text{SNR}_I = I/\delta I$) and polarized intensity ($\text{SNR}_{\text{PI}} = \text{PI}/\delta \text{PI}$). The criteria include $\text{SNR}_I > 10$ and $\text{SNR}_{\text{PI}} > 3$. The 20MC, 50MC, and CND are marked by green, orange, and cyan dashed circles, respectively. Continuum emission closer to the centers of the clouds exhibits lower polarization fractions compared to that observed at the edges.

In Figure 2, we calculate the difference in the magnetic field position angle between those derived from the polarization at 450 and $850 \mu\text{m}$, ranging from -90° to 90° , and investigate its dependence on the SNR_{PI} . The angle difference $\Delta\theta$ between two selected position angles, θ_1 and θ_2 , is calculated using the

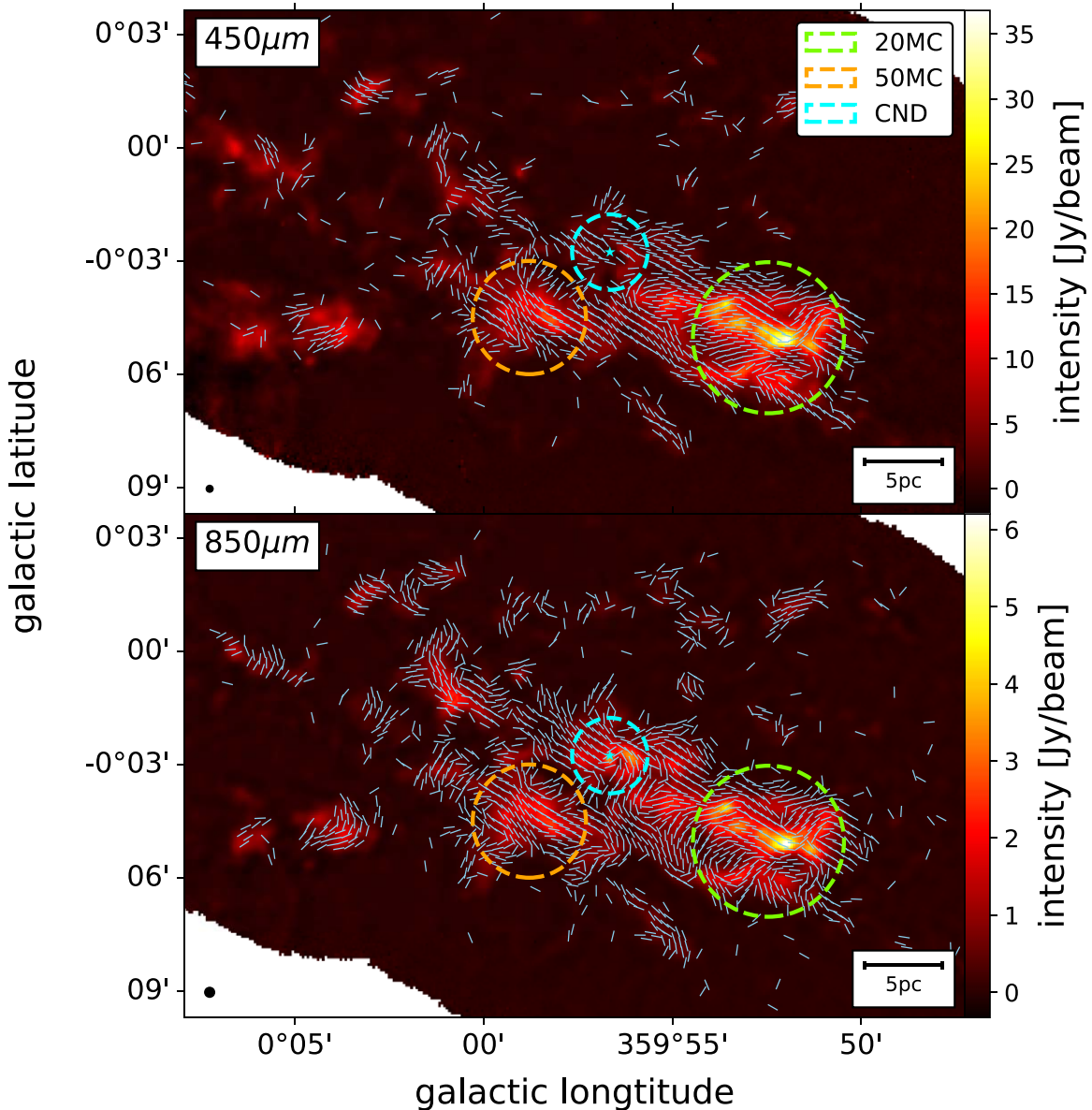


Figure 1. The magnetic field orientations sampled on a $12''$ grid overlaid on the Stokes I maps containing CO contamination sampled on a $4''$ grid at 450 and 850 μm . White segments represent magnetic field orientations determined by rotating the polarization orientations by 90° . The polarization half-vectors are selected by the SNR criteria of Stokes I and polarized intensity: $\text{SNR}_I > 10$ and $\text{SNR}_{\text{PI}} > 3$. All half-vectors are of uniform length. The orange dashed circles mark the position of the 50MC, and the green dashed circle marks the position of the 20MC. The position of the CND is marked by cyan dashed circle with the central star marking the location of Sgr A*.

following equation from Planck Collaboration et al. (2016):

$$\Delta\theta(\theta_1, \theta_2) = \frac{1}{2} \arctan\left(\frac{\sin 2\theta_1 \cos 2\theta_2 - \cos 2\theta_1 \sin 2\theta_2}{\cos 2\theta_1 \cos 2\theta_2 + \sin 2\theta_1 \sin 2\theta_2}\right). \quad (6)$$

Here, θ_1 is the position angle derived from the polarization at 450 μm , and θ_2 is the position angle derived from the polarization at 850 μm . We further estimate the average position angle difference, $\Delta\theta$, and the standard deviation, $\sigma_{\Delta\theta}$, for each 5 unit bin along the axis. The shaded regions in Figure 3 mark the area between $\Delta\theta - \sigma_{\Delta\theta}$ and $\Delta\theta + \sigma_{\Delta\theta}$. The shaded areas are mostly located within the $\Delta\theta$ range of -25° to 25° when the SNR_{PI} is higher than 15 for the 450 μm data and higher than 30 for the 850 μm data, respectively. This indicates

that the magnetic fields inferred from the 450 and 850 μm data exhibit greater consistency in regions with high- SNR_{PI} . It implies that the polarized emissions at these two wavelengths originate in similar regions and are less contaminated by the LOS material, consistent with our assumption. Additionally, low- SNR_{PI} , for example where $\text{SNR}_{\text{PI},850 \mu\text{m}}$ is below about 30, exhibits more significant position angle differences.

The evident angle difference possibly arises from a combination of astrophysical and technical factors, including the beam size discrepancies and the inherent challenges of 450 μm observations. In general, dense molecular clouds in the CMZ likely have multiple layers of gas and dust, each with a distinct magnetic field orientation, such that the observed polarization angle reflects the vector sum of these layers. If the LOS contributions at 450 μm differ from those at 850 μm —for instance, if the 450 μm emission selectively samples warmer

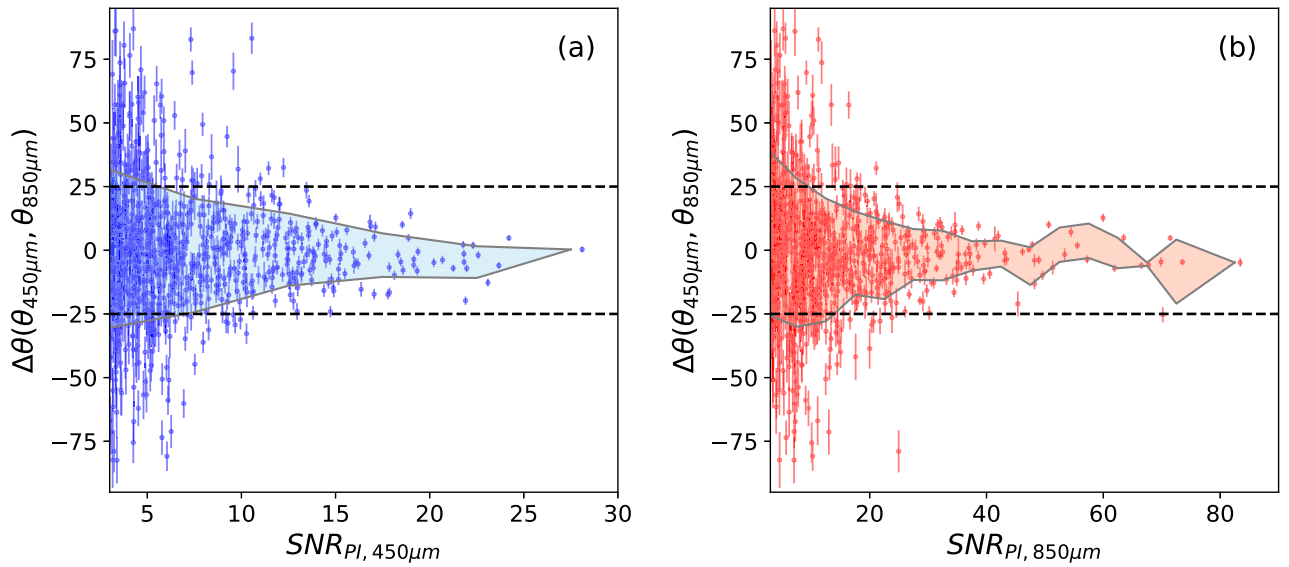


Figure 2. Dependence of the magnetic field position angle difference on the SNR of the polarization intensity derived from (a) 450 μm and (b) 850 μm observations. The polarizations are selected by the SNR criteria: $\text{SNR}_I > 10$ and $\text{SNR}_{PI} > 3$. The scatter points represent the position angle differences with corresponding uncertainties for each pixel. The shaded regions in Figure 3 mark the area between $\overline{\Delta\theta} - \sigma_{\Delta\theta}$ and $\overline{\Delta\theta} + \sigma_{\Delta\theta}$, where $\overline{\Delta\theta}$ and $\sigma_{\Delta\theta}$ indicate the position angle difference and the standard deviation for each 5 unit bin along the axis. The dashed lines show the range of $\Delta\theta$ from -25° to 25° .

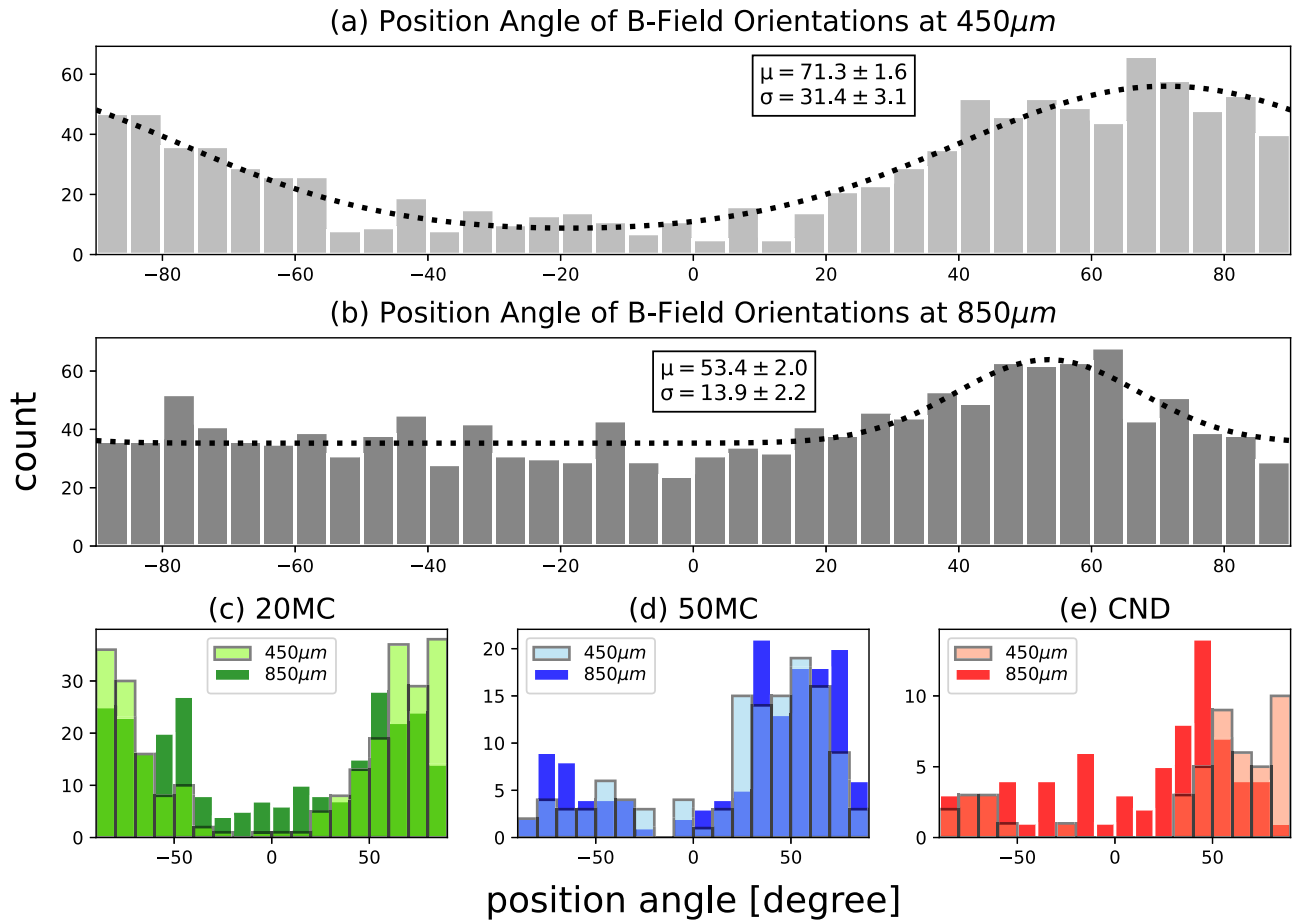


Figure 3. Histogram of the magnetic field orientations derived from (a) 450 μm and (b) 850 μm polarization observations. The polarization half-vectors are selected by the criteria $\text{SNR}_I > 10$ and $\text{SNR}_{PI} > 3$. The dark dotted lines show the fitting results from a single Gaussian model. Panels (c), (d), and (e) show the histograms of the magnetic fields position angles within the circular regions toward the 20MC, 50MC, and CND, as depicted in Figure 1, respectively. Magnetic field position angles range from -90° to 90° , with 0° pointing north in Galactic coordinates and $\pm 90^\circ$ aligned with the Galactic plane.

layers—then the measured polarization angles need not be consistent with each other. Given the nature of CMZ gas, especially toward the CNL, some polarization segments at $850\ \mu\text{m}$ could even trace synchrotron emission (see, e.g., Figure 2(b) in K. Sato et al. 2024). Verifying each polarization segment goes beyond the scope of this overview paper, but a paper addressing these topics is currently in preparation by BISTRO members (R. S. Furuya 2025, in preparation).

D. Paré et al. (2024) confirmed a bimodal distribution on the histogram of the CMZ magnetic field orientations using SOFIA/HAWC+ polarization observations at $214\ \mu\text{m}$. Their results revealed two distinct magnetic field components: one aligned parallel, and the other aligned perpendicular to the Galactic plane. In Figure 3, we show histograms of the magnetic field orientations, which are selected by the criteria $\text{SNR}_I > 10$ and $\text{SNR}_{\text{PI}} > 3$, for the entire region at 450 and $850\ \mu\text{m}$ in panels (a) and (b), respectively, as well as for each distinct structure in panels (c), (d), and (e). The position angles for the 20MC, 50MC, and CNL are extracted within three circular regions with radii of $1'$ ($\sim 2.4\ \text{pc}$), $1.5'$ ($\sim 3.6\ \text{pc}$), and $2'$ ($\sim 4.8\ \text{pc}$), respectively, as shown in Figure 1. The magnetic field orientations do not show significant differences in these regions. Our data, however, do not display a similar bimodal distribution at both 450 and $850\ \mu\text{m}$; instead, they exhibit only one dominant direction. Therefore, we apply a single-Gaussian model to fit the data, as described by the following equation:

$$y = H + Ae^{-\frac{(x-\nu)^2}{2\sigma^2}}, \quad (7)$$

where x is the polarization angle ranging from -90° to $+90^\circ$, y is the count value, H is the offset above zero, A is the amplitude of the Gaussian peak, ν is the mean orientations, and σ is the standard deviation of the Gaussian peak, which indicates how the position angle distribution spreads.

The best-fit Gaussian peaks are located at position angles of 71.3° and 53.4° with σ of 31.4° and 13.9° for the 450 and $850\ \mu\text{m}$ data, respectively, as shown by the dashed lines in Figure 3 panels (a) and (b). The fitting result for the 450 μm data indicates that the overall magnetic fields have a position angle difference of $\sim 20^\circ$ relative to the Galactic plane. This value is consistent with one of the components in the bimodal distribution proposed by D. Paré et al. (2024). In contrast, the magnetic field derived from $850\ \mu\text{m}$ polarization observations tends to exhibit a larger position angle difference ($\sim 40^\circ$) relative to the Galactic plane. Additionally, the histogram of the $850\ \mu\text{m}$ data shows a general offset H of ~ 35 above zero on the y -axis, suggesting a more complex or disordered magnetic field morphology. In panels (c), (d), and (e), we present histograms of the magnetic field position angles within the circular regions corresponding to the 20MC, 50MC, and CNL, all of which are bright dust structures in the inner region of the CMZ, as shown in Figure 1.

Figure 4 shows the contamination level by ^{12}CO (6–5) and ^{12}CO (3–2) proposed by H. Parsons et al. (2018) in panels (a) and (b). In the vicinity of the CNL, dust observations are significantly impacted by CO line emission. We use these maps to eliminate the impact of CO emission. Figure 5 gives close-ups of the 20MC, 50MC, and CNL to highlight the structure of their magnetic fields. Magnetic field orientations are represented by orange and yellow line segments with SNR criteria of polarization intensity, $\text{SNR}_{\text{PI}} > 3$ and $2 \leq \text{SNR}_{\text{PI}} < 3$, respectively. The lengths of the line segments in Figure 5 are proportional to the

polarization fractions, which are obtained using the CO-removed intensity maps. The position angles reveal a highly ordered magnetic field morphology within each region. In the 20MC region, the magnetic field orientations align with the Galactic Plane, as indicated by the peak in the histogram in panel (c) of Figure 4 near a position angle of 90° . From panels (a) and (b) in Figure 5, the field morphology appears to follow the skeleton of the dust structures. Near the 50MC, the magnetic field points northwest in the northern region and northward in the southern region, with a clear transition at the center. In the vicinity of the CNL, a distinct spiral magnetic field morphology is observed, with its center point roughly consistent with Sgr A*.

3.1.2. Comparison of B Field Position Angles in the CNL with SCUPOL Observations

The spiral magnetic field structure (panel (a) and panel (b) in Figure 5) had been previously observed at $850\ \mu\text{m}$ using the polarimeter SCUPOL on the JCMT (P.-Y. Hsieh et al. 2018). In Figure 6, we make a comparison between the magnetic field orientations obtained with POL-2 observations (red segments) and those with SCUPOL observations (blue segments). We refer to the schematic of the CNL given by P.-Y. Hsieh et al. (2019) to define the boundary. The CNL is thought to be a torus inclined at an angle of $\sim 70^\circ$ along the axis parallel to the Galactic Plane. We define the boundary of the CNL as an ellipse with a major axis of 4 pc and an aspect ratio of 0.34. The ellipse is centered on Sgr A* and aligned with the Galactic Plane. Between the POL-2 and SCUPOL observations, the magnetic field position angles are similar in the elliptical region, except for the southeastern part.

We investigated the variation in magnetic field position angles with azimuthal angle in the CNL, as shown in Figure 7. To illustrate the difference between the position angles observed by POL-2 and SCUPOL, we present the data with different SNR of the polarization intensity using different colors. The azimuthal angle ranges from -180° to 180° , increasing counterclockwise, with the north direction in the Galactic coordinates defined as 0° . To analyze the trend of position angle variation within the azimuthal angle range of -90° , where the position angle increases from $\sim 0^\circ$ as the azimuthal angle increases, we show the position angle in the range of 0° to 180° . In the southeastern region (between -90° and -180°), the position angles from the POL-2 and SCUPOL observations are not well matched. The SNR_{PI} of POL-2 $850\ \mu\text{m}$ observations are generally higher than 3 in this region. The referring magnetic field position angles rotate counterclockwise as the azimuthal angle increases from -180° to -90° , corresponding to the red points rising between the dashed lines. SCUPOL observations with $\text{SNR}_{\text{PI}} > 3$ are in good agreement with our data. Data points with $1 \leq \text{SNR}_{\text{PI}} < 3$, however, are aligned with different orientations.

Our higher quality observations consequently reveal a more pronounced left-handed spiral morphology in the CNL.

3.2. Magnetic Field Strength

We use the DCF method (L. Davis 1951; S. Chandrasekhar & E. Fermi 1953) to estimate the POS magnetic field strength by assuming the equipartition between the kinetic energy of turbulence and the fluctuating magnetic energy. The POS uniform magnetic field strength is estimated with

$$B_{\text{POS}} = Q' \sqrt{4\pi\rho} \frac{\sigma_\nu}{\sigma_\theta}. \quad (8)$$

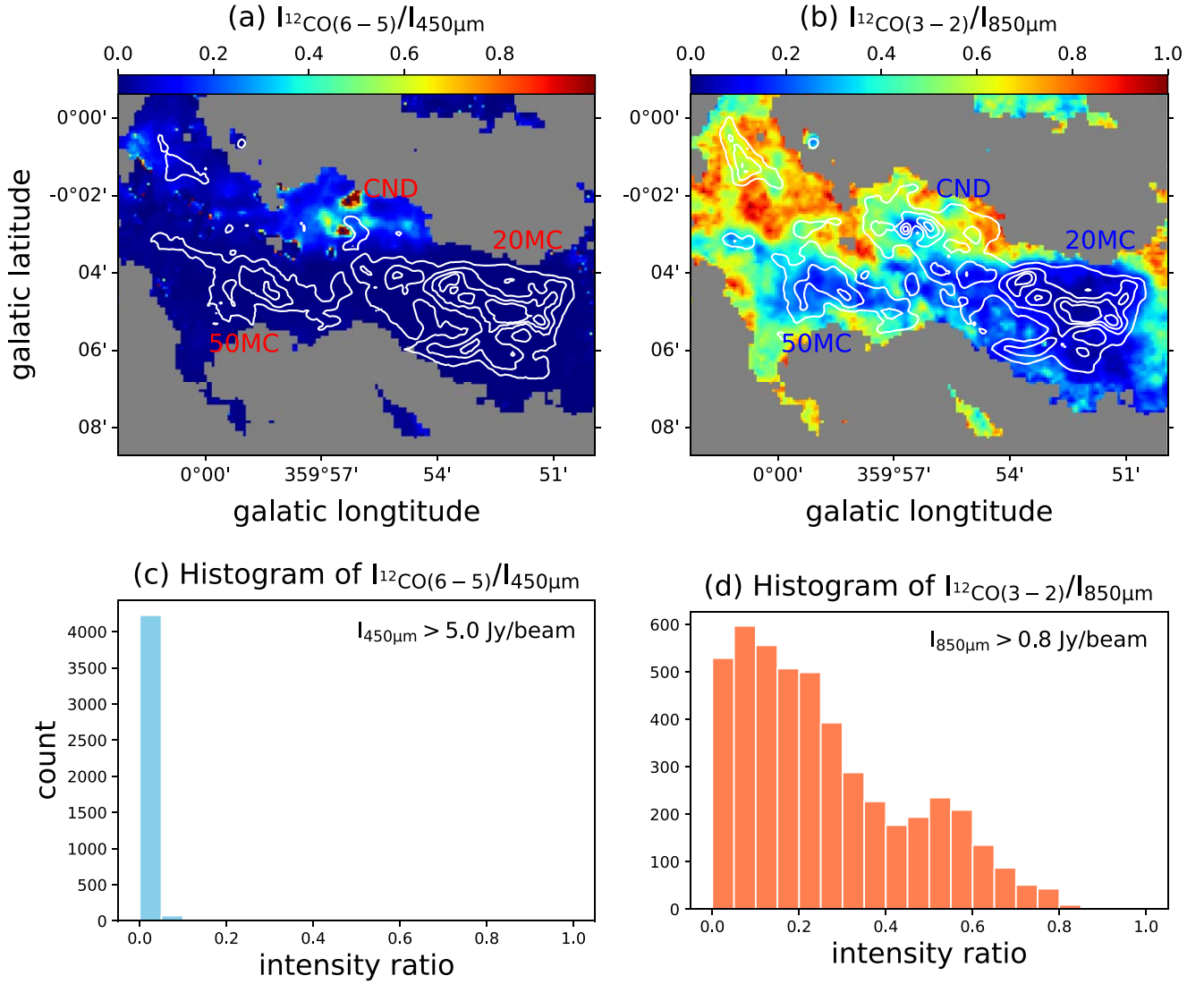


Figure 4. The intensity ratio between the CO gas emission and continuum observations, indicating the contamination level by (a) ^{12}CO (6–5) and (b) ^{12}CO (3–2). The contours show the $450\ \mu\text{m}$ intensities of [5, 10, 15, 20] Jy beam^{-1} in panel (a) and the $850\ \mu\text{m}$ intensities of [0.8, 1.6, 2.4, 3.2] Jy beam^{-1} in panel (b). Panel (c) illustrates the ^{12}CO (6–5) contamination levels for $450\ \mu\text{m}$ while $I_{450\ \mu\text{m}} > 5\ \text{Jy beam}^{-1}$. Panel (d) shows the ^{12}CO (3–2) contamination levels for $850\ \mu\text{m}$ while $I_{850\ \mu\text{m}} > 0.8\ \text{Jy beam}^{-1}$.

Here, ρ is the gas density ($\rho = \mu_{\text{H}_2} m_{\text{H}} n(\text{H}_2)$), where $n(\text{H}_2)$ is the number density of molecular hydrogen, μ_{H_2} is the mean molecular weight per hydrogen molecule, and m_{H} is the mass of hydrogen. We adopt $\mu_{\text{H}_2} = 2.86$ from J. M. Kirk et al. (2013); σ_v is the nonthermal velocity dispersion in the gas; σ_θ is the angular dispersion of the polarization position angles; and Q' represents a dimensionless factor of an order of unity, which corrects for the bias in magnetic field strength on scales smaller than the beam. According to J. Liu et al. (2022), we adopt $Q' \approx 0.28$ with 50% uncertainty.

R. M. Crutcher (2004) also suggested a statistical correction to approximate the total magnetic strength in the three-dimensional space

$$|B_{\text{tot}}| \approx \frac{4}{\pi} B_{\text{pos}}. \quad (9)$$

Therefore, calculating the magnetic field strength requires values for number density, angular dispersion, and velocity dispersion.

3.2.1. Volume Density

As the first step in determining the volume density, we calculate the column density using the CO-removed intensities at 450 and $850\ \mu\text{m}$. Under the assumption that the dust emission is optically thin and follows a graybody distribution in the submillimeter observations, the column density (N_{H_2}) can be estimated by the opacity spectral index (β), temperature (T), and observed flux density (S_ν^{beam}), as follows:

$$N_{\text{H}_2} = \frac{S_\nu^{\text{beam}}}{\Omega_A \mu_{\text{H}_2} m_{\text{H}} \kappa_\nu B_\nu(T)}, \quad (10)$$

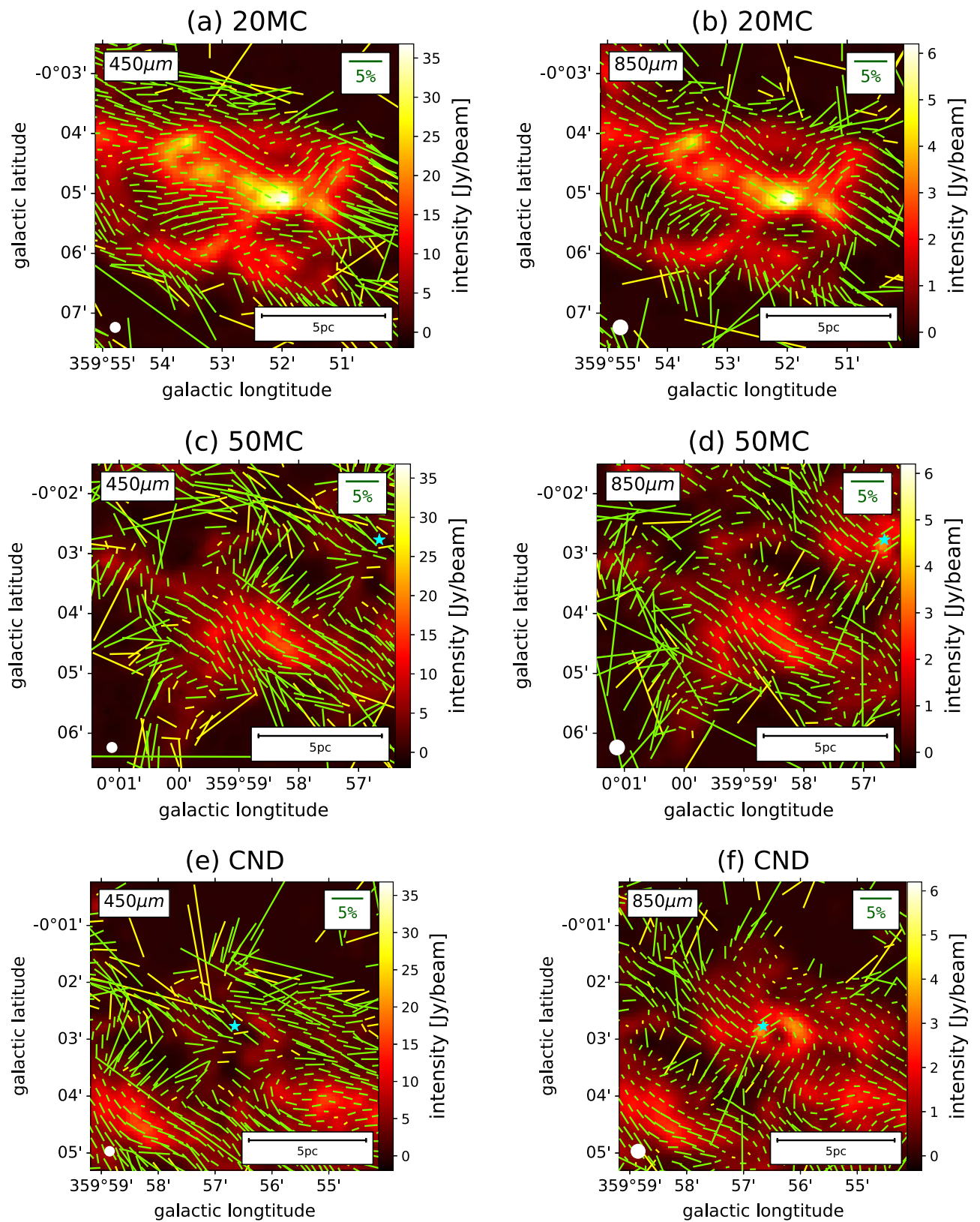


Figure 5. Zoomed-in maps of three distinct regions: 20MC in panels (a) and (b), 50MC in panels (c) and (d), and CND in panels (e) and (f), at $450\mu\text{m}$ and $850\mu\text{m}$, respectively. Magnetic field orientations are represented by line segments, with their lengths proportional to the polarization fraction for an SNR higher than 3 (green) or between 2 and 3 (yellow), respectively. The lengths of the half-vectors are proportional to the polarization fraction obtained using the CO-removed intensity maps.

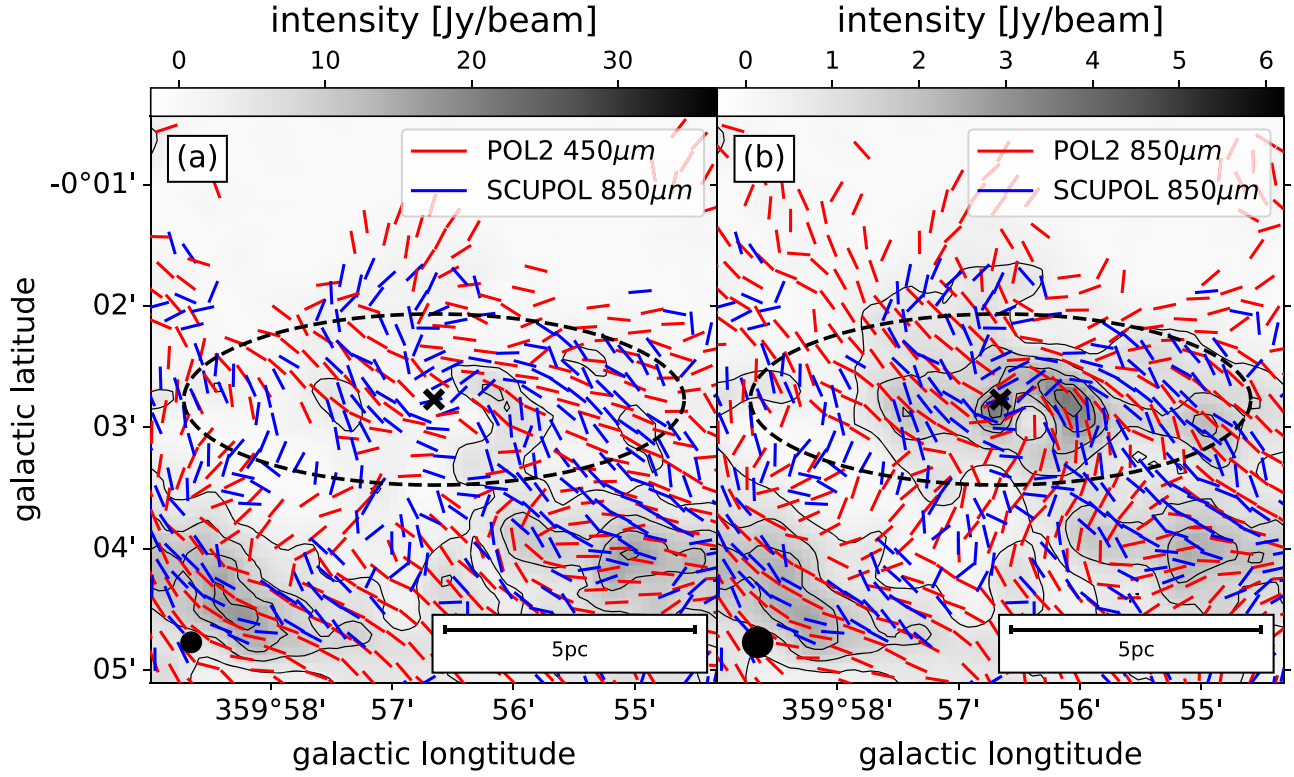


Figure 6. Magnetic field orientations determined by BISTRO 450 and 850 μm observations (red segments) compared to those determined by SCUPOL 850 μm observations (blue segments) in the vicinity of the CND. All segments are of uniform length. Both POL-2 and SCUPOL polarization data are selected by the criteria of $\text{SNR}_I > 10$ and $\text{SNR}_{PI} > 3$. The dashed ellipse, with a 4 pc major axis aligned with the Galactic Plane and an aspect ratio of 0.34, outlines the boundary of the CND.

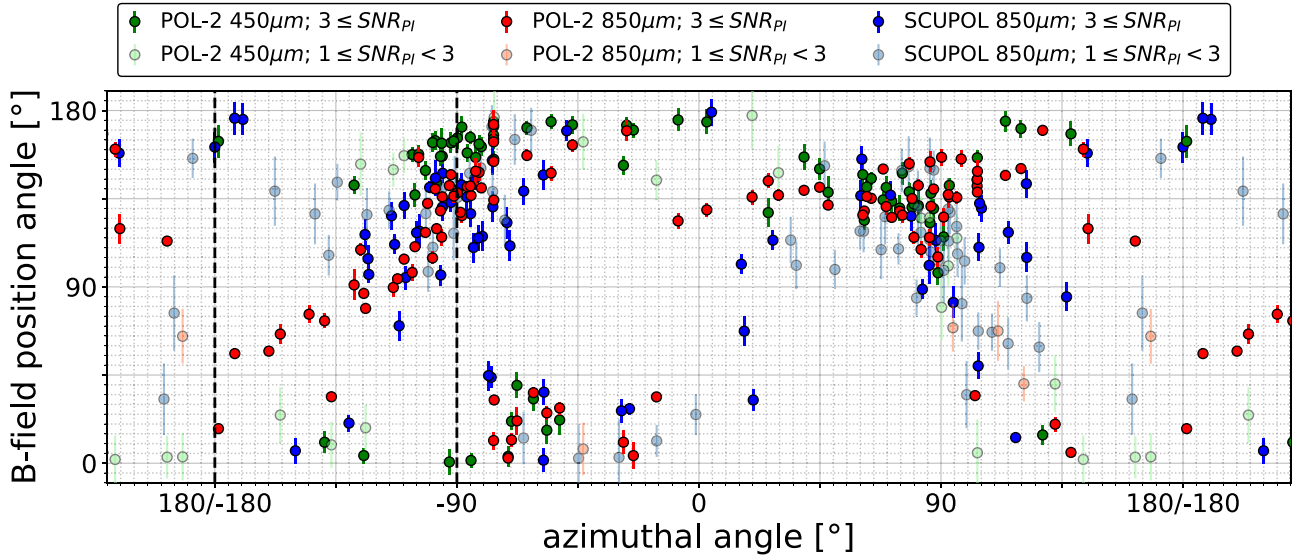


Figure 7. The magnetic field position angle vs. azimuthal angle in the CND. Azimuthal angle ranges from -180° to 180° with the north direction in Galactic coordinate defined as 0° . Position angles are displayed in the range from 0° to 180° . The data enclosed between the two dashed lines represent observations from the southwest region related to Sgr A*. The different colors of the data points represent various observations and separate the data into polarization intensity SNR ranges of $1 \leq \text{SNR}_{PI} < 3$ and $\text{SNR}_{PI} \geq 3$.

where

$$B_\nu(T) = \frac{2h\nu^3}{c^2} \frac{1}{\exp(h\nu/kT) - 1}, \quad (11)$$

and

$$\kappa_\lambda = \kappa_0 \left(\frac{1000 \mu\text{m}}{\lambda} \right)^{-\beta}. \quad (12)$$

Here, Ω_A is the solid angle of the beam. We adopt the dust opacity at the wavelength of 1000 μm , $\kappa_0 = 0.0137 \text{ cm}^2 \text{ g}^{-1}$ (V. Ossenkopf & T. Henning 1994), as the reference in Equation (12), assuming the gas-to-dust mass ratio of 100.

We cannot estimate the column density based solely on the BISTRO observations at two wavelengths because there are three unknowns, including N_{H_2} , β , and T . Therefore, we utilize the continuum data at wavelengths of 160, 250, 350, and

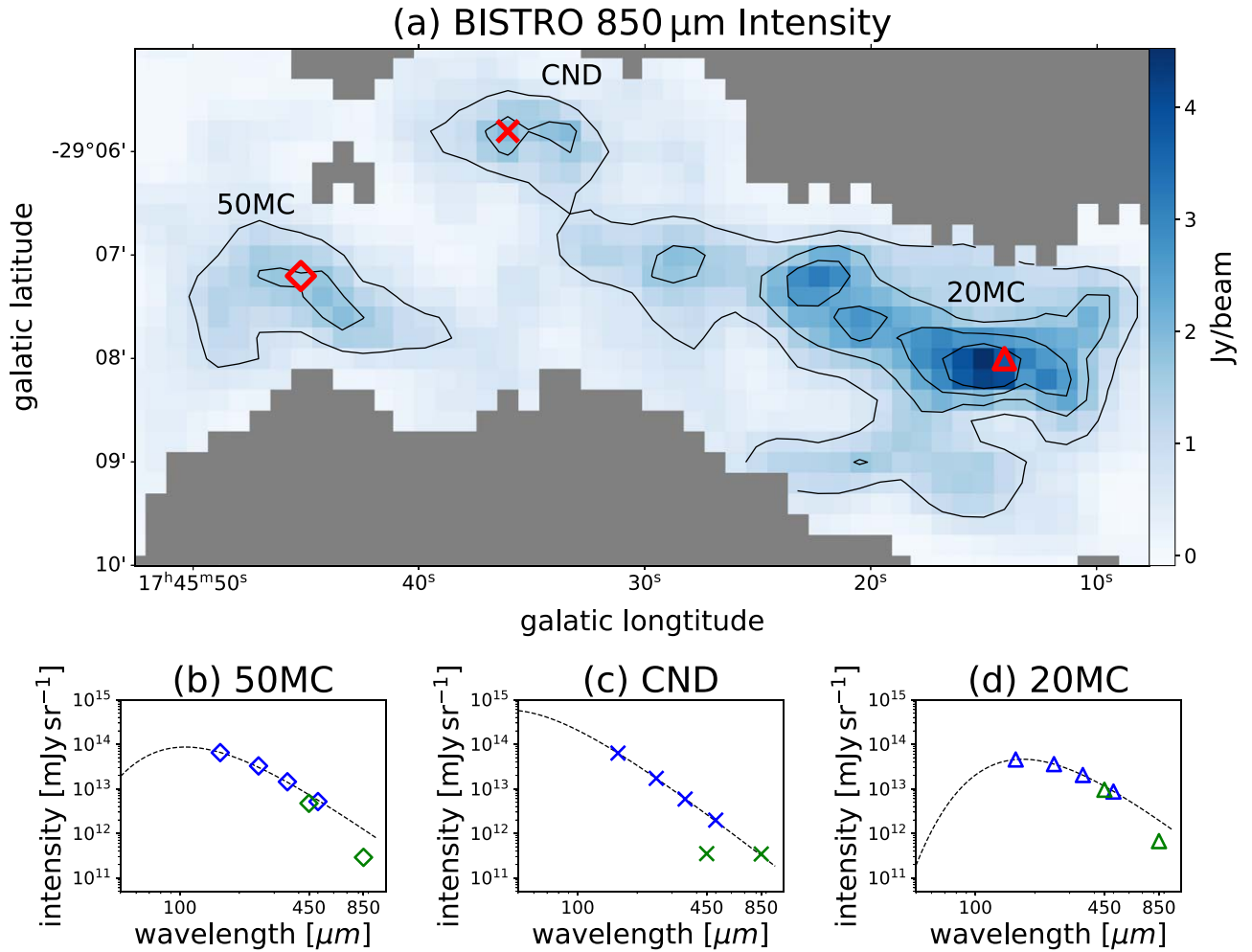


Figure 8. Three cases of the SED fitting toward the 50MC, CND, and 20MC, shown in panels (b), (c), and (d). The panel (a) shows the CO-removed intensity at $850\ \mu\text{m}$ with contours corresponding $[0.8, 1.6, 2.4, 3.2]\ \text{Jy beam}^{-1}$. Positions in the vicinity of 20MC, 50MC, and CND are selected as examples and shown in right panel. The right panel displays the SED fitting results (black dashed line) using Hi-GAL observations, with Hi-GAL data represented in blue and CO-removed BISTRO intensity in green. In panels (b), (c), and (d), all uncertainties are less than 1% and are therefore not shown.

$500\ \mu\text{m}$ from the Hi-GAL survey, which used the Herschel Space Observatory to scan the entire Galactic Plane (K. A. Marsh et al. 2017), to fit the opacity spectral index and temperature using Equation (10). Since the BISTRO continuum intensities at 450 and $850\ \mu\text{m}$ are not consistent with the SED determined by the Hi-GAL data, we did not use them simultaneously for SED fitting. In Figure 8, we convolve all intensity maps with the beam size of Hi-GAL data at $500\ \mu\text{m}$ ($36''$) and display the intensity profiles with five different wavelengths from both of Hi-GAL (blue) and BISTRO observations (green) at three distinct positions in the vicinity of the 20MC, 50MC, and CND. The black dashed lines denote the fitting results using solely the Hi-GAL data by the Equation (10), revealing obvious differences with the BISTRO observations. The lack of consistency between the BISTRO and Hi-GAL data on the SED is caused by SCUBA-2 measurements missing flux from large-scale structures.

Figure 9 displays the fitting results for the opacity spectral index β , the temperature, and the column density. The β value ranges from approximately 1.0 to 2.8, with the lowest value observed around the CND. The temperature is higher closer to the Galactic center and decreases near the 20MC and 50MC. Using this temperature map, the optical depth is ~ 0.1 at $450\ \mu\text{m}$

and ~ 0.01 at $850\ \mu\text{m}$, which is consistent with the assumption that the dust emission is optically thin. We apply the fitted β and T to estimate the column density using the BISTRO observations at both 450 and $850\ \mu\text{m}$ wavelengths, shown in Figure 10. Near the 20MC and 50MC, the column density exceeds $10^{22}\ \text{cm}^{-2}$, and the distributions have similar structures between the wavelengths of 450 and $850\ \mu\text{m}$. In the vicinity of the CND, the column density maps show distinct ringlike structures at both 450 and $850\ \mu\text{m}$, which are consistent with the scenario proposed by previous studies (e.g., P.-Y. Hsieh et al. 2019).

To estimate the average physical properties of the 20MC, 50MC, and CND in the following sections (e.g., $n(\text{H}_2)$, σ_θ), we need to define the boundary of each structure. We use the Python package *astrodendro*⁴¹ to compute dendrograms and define the boundaries of the 20MC and 50MC based on the column density maps at both wavelengths. A lower-column density limit of $10^{22}\ \text{cm}^{-2}$ is applied for the $450\ \mu\text{m}$ data and $5 \times 10^{21}\ \text{cm}^{-2}$ for the $850\ \mu\text{m}$ data. Due to the obvious difference in the CND boundaries determined by *astrodendro* at 450 and $850\ \mu\text{m}$, we adopt the elliptical boundary defined in

⁴¹ <http://www.dendrograms.org/>

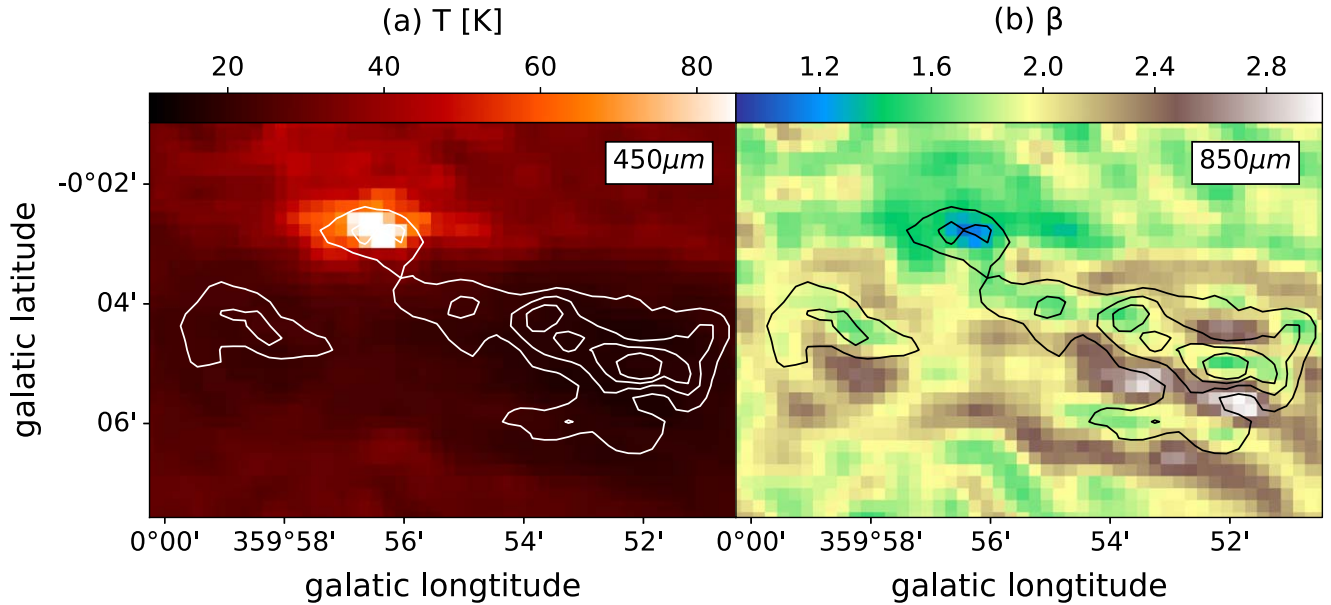


Figure 9. The temperature, opacity spectral index, and column density maps determined by SED fitting using Hi-GAL observations at wavelength of 160, 250, 350, 500 μm . The contours show the CO-removed intensities at 850 μm with the values of [0.8, 1.6, 2.4, 3.2] Jy beam^{-1} . The black cross is the position of the Sgr A*.

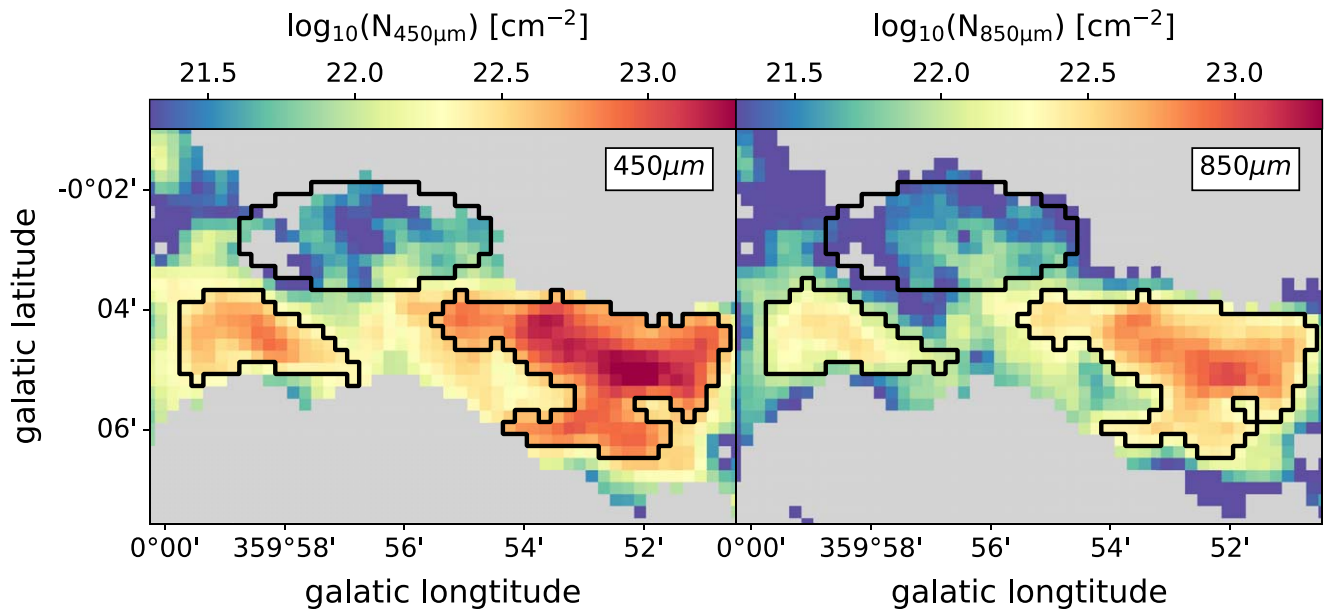


Figure 10. Column density maps estimated by the BISTRO observations at 450 and 850 μm using the temperature and opacity spectral index parameters shown in Figure 9. Black contours depict the boundaries of the 20MC, 50MC, and CND.

Section 3.1.2. The black contours in Figure 10 depict the boundaries of the 20MC, 50MC, and CND.

To calculate $n(\text{H}_2)$, the LOS spatial depth is necessary. S. Molinari et al. (2011) suggested that there is a 100 pc elliptical and twisted ring around the Galactic center, enclosing the 20MC and 50MC. We model the material distribution around these two massive molecular clouds as cylinders lying on the POS and manually adjust the cylinder radii to encompass the structures determined by astrodendro. The radii and lengths of the cylinders are 4.4 and 15.0 pc for the 20MC, and 3.0 and 9.6 pc for the 50MC, respectively. Using these models, we calculate the LOS distance pixel by pixel and estimate the number density around the 20MC and 50MC. For the CND region, with the elliptical boundary defined in Section 3.1.2, we use the typical thickness of

~ 0.4 pc as suggested by H. M. Latvakoski et al. (1999) to calculate the number density. These LOS distances are considered the 50% errors. The number density maps in the vicinity of the 20MC, 50MC, and CND are shown in Figure 11. Table 2 lists the average number densities for these three structures at 450 and 850 μm . The uncertainty in the number density is calculated by propagating the uncertainties from the observational data, temperature, and opacity spectral index. The latter two are based on the 1σ errors from the SED fitting.

3.2.2. Angular Dispersion

We utilize the “unsharp masking” method, as introduced by K. Pattle et al. (2017) to calculate the angular dispersion of the

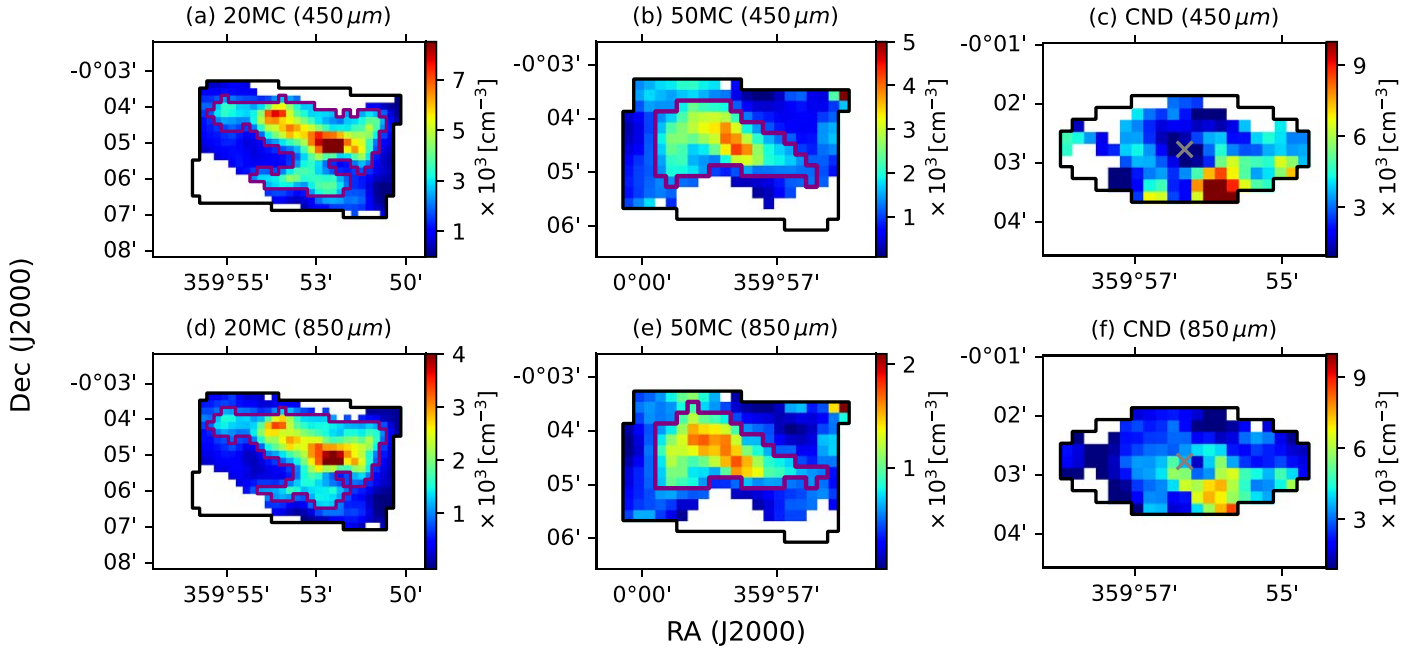


Figure 11. The number density maps in different regions at 450 μm (a) to (c) and 850 μm (d) to (f), overlaid with the corresponding column density maps. Purple solid lines show the structures of 20MC and 50MC determined by astroendro. Black solid lines shows the boundaries of the cylinder and ellipse models, used to determine the LOS spatial depth.

Table 2

Values of Number Density, FWHM Velocity Dispersion, Angular Dispersion, and Dust Temperature Used to Estimate the Magnetic Field Strengths Using the DCF Method within the Regions of 20MC, 50MC, and CND

Region	$n(\text{H}_2)$ (cm^{-3})		σ_v (km s^{-1})		σ_θ (deg)		T (K)	
	450 μm	850 μm	450 μm	850 μm	450 μm	850 μm	450 μm	850 μm
20MC	4437 (572)	2141 (235)	11.3 (0.7)	10.3 (0.6)	9.3 (0.4)	8.4 (0.4)	18.6 (1.2)	18.2 (1.2)
50MC	2624 (471)	1335 (192)	10.3 (0.4)	10.2 (0.5)	6.7 (0.8)	5.7 (0.7)	23.0 (1.9)	22.9 (1.9)
CND	3464 (724)	2897 (616)	31.8 (6.6)	31.7 (6.7)	10.4 (0.7)	10.9 (0.4)	52.7 (36.1)	52.7 (36.1)

Note. Values in parentheses indicate the corresponding uncertainties. Uncertainties are calculated by propagating the uncertainties of the observational data, 1σ errors from the Hi-GAL SED fitting, and 1σ errors from the C^{18}O (1–0) spectrum fitting.

magnetic fields for the turbulent component at 450 and 850 μm . They determined the large-scale magnetic field morphology by smoothing the position angles using a boxcar average. The size of the boxcar filter is chosen so that the smoothing length is smaller than the radius of curvature of the magnetic field morphology. If there is any pair of the polarization position angles in the boxcar with angle difference higher than 90° , this pixel at the center of the boxcar will be masked out because the magnetic field is too distorted to determine a mean direction (see K. Pattle et al. 2017 for details). Then, the mean directions are subtracted from the original ones to obtain the angle differences, which are regarded as the turbulent component of the magnetic field morphology. The angular dispersion is the standard deviation of the angle differences within a specific region.

We select polarization data with a pixel size of $12''$ at both 450 and 850 μm , using the criteria $\text{SNR}_I > 10$ and $\text{SNR}_{\text{PI}} > 3$. To determine the size of the boxcar filter, we estimate the radii of curvatures, using the following formula suggested by

P. M. Koch et al. (2012):

$$C \equiv \frac{1}{R} = \frac{2}{d} \cos\left(\frac{1}{2}[\pi - \Delta\text{PA}]\right), \quad (13)$$

where C is the curvature; R is the radius of curvature; and d and ΔPA are the distance and the position angle difference between two adjacent pixels, respectively. After investigating the curvatures of the magnetic field morphology, we adopt 3 pixels (~ 1.5 pc) as the length of the boxcar filter, which is smaller than most of the radii of local curvatures at both 450 and 850 μm . We smooth the magnetic field position angles using a 3×3 boxcar filter across the entire region, and produce the residual maps. If the valid data points are less than 4 within the number of boxcar filter, this position will be masked out. Figures 12 and 13 display the results at 450 and 850 μm , respectively. The pixels that have been masked out during the process are shown in gray. The line segments and the color maps display the position angles simultaneously. The angular

dispersion is obtained by calculating the standard deviation of the position angle differences within the corresponding boundary. Table 2 shows the angular dispersion in the 20MC, 50MC, and CNL at 450 and 850 μm . The uncertainty in the angular dispersion is estimated by propagating the observational uncertainties.

3.2.3. Velocity Dispersion

We calculate the average velocity dispersion using the C^{18}O (1–0) observations obtained from NRO with a resolution of $15''$, assuming that the molecular emission traces approximately the same structures as the submillimeter continuum emission. In Figure 14, we mask values below 3 times the noise level over the spectral line and calculate the zeroth and first moment maps to investigate the integrated intensity, intensity-weighted velocity, and velocity dispersion, respectively. In panel (a), we observe bright gas emission within the 20MC and 50MC regions, with fainter emission in the CNL. Panel (b) shows a gradual change in velocity. The C^{18}O (1–0) spectra, however, exhibit multiple emission peaks in some regions, leading to overestimations of the velocity dispersion derived from the second moment map. We interpret that the multiple components of the spectrum are being caused by the several structures along the LOS that have different gas dynamics with distinct mean velocity and velocities' dispersions.

Accordingly, we fit the spectra with multiple Gaussian profiles to determine the brightness, mean velocity, and velocity dispersion of each emission peak. The goodness of the fitting is judged by the chi-squared test. We perform the spectral line fitting pixel by pixel. Each spectrum is fitted first by a single Gaussian profile, and the reduced chi-squared value is calculated. If the reduced chi-squared value is greater than 2, we add one more Gaussian profile. This process iterates until the reduced chi-squared value is lower than 2 or the number of Gaussian profiles exceeds 6. In the event those criteria cannot be met, we assume the spectrum is too noisy to be analyzed.

Subsequently, we analyze the fitting results in the position–velocity (PPV) space and attempt to distinguish different gas structures. We assume that the emission peaks of the spectra correspond to distinct gas structures along the LOS. First, we sort the fitting results into different groups based on the number of components. One-component spectra account for $\sim 50\%$, $\sim 50\%$, and $\sim 70\%$ of the area within the boundaries of 20MC, 50MC, and CNL, respectively. These components in PPV space exhibit smooth velocity variations, suggesting a similar kinematic structure along the LOS, which we define as the “first layer structure.”

Then, we investigate spectra with several components adjacent to pixels with the first layer structure by calculating the velocity differences between these components and the component of the first layer structure. The component with the minimum velocity difference is considered to connect to the first layer structure in the PPV space, if the velocity difference is smaller than the full width at half-maximum (FWHM) of the component of the first layer structure. We continue iterating this process until no component is classified as part of the first layer structure. As a result, all components are separated into two groups: the first layer structure and the remaining structures. The classification results are shown in Figure 15. In panel (a) of Figure 15, the first layer structure covers the regions of the 20MC, 50MC, and CNL. We can further investigate other gas structures using the

remaining components (panel (b) in Figure 15), but these are too fragmented in PPV space to define coherent gas structures.

We adopt the first layer structure in PPV space as indicative of the typical gas motion. Figure 16 shows the comparison between the velocity dispersion maps determined by the second moment map (panel (a)) and our analysis (panel (b)). The velocity dispersions in panel (b) are smaller than those in panel (a) and exhibit more coherence due to the elimination of minor components. We estimate the nonthermal velocity dispersion by subtracting the thermal component from the C^{18}O velocity dispersion using the relation

$$\sigma_v^2 = \sigma_{v,\text{C}^{18}\text{O}}^2 - \frac{k_{\text{B}}T}{m_{\text{C}^{18}\text{O}}}, \quad (14)$$

where σ_v is the nonthermal gas velocity dispersion, $\sigma_{v,\text{C}^{18}\text{O}}$ is the velocity dispersion of the C^{18}O (1–0), and $m_{\text{C}^{18}\text{O}}$ is the mass of the C^{18}O molecule. The temperature is taken from the dust temperature shown in Figure 9 under the assumption the dust and gas are in thermal equilibrium. By using the boundaries defined in Section 3.2.1 for the 20MC, 50MC, and CNL, we estimate the average velocity dispersion within these regions, and present the results in Table 2. The uncertainties in the velocity dispersions are estimated by propagating the observational uncertainties and the 1σ errors from the spectrum fitting.

The σ_v in the CNL is significantly larger than that in the 20MC and 50MC. M. S. Akshaya & T. Hoang (2024) obtained a velocity dispersion in the CNL that is approximately one-third of our value by decomposing the CHIMPS2 ^{12}CO (3–2) spectra using more Gaussian components. These ^{12}CO (3–2) observations are brighter than the C^{18}O (1–0) emissions measured by NRO. We attempted to decompose the CHIMPS2 ^{12}CO (3–2) spectra but encountered degeneracy issues and possible absorption in the spectra. Therefore, we continue to use the CHIMPS2 C^{18}O (1–0) as the tracer to determine σ_v , while cautioning that the decomposition process has inherent limitations.

3.2.4. Results of DCF Method

The average values and the corresponding uncertainties of the $n(\text{H}_2)$, σ_θ , and σ_v within the structures boundaries of 20MC, 50MC, and CNL are shown in Table 2 (note that the boundaries determined using 450 and 850 μm intensity maps are different). We use these results to estimate the POS magnetic field strengths and infer the statistical three-dimensional magnetic field strengths using Equations (8) and (9), respectively. The POS magnetic field strengths derived from the 450 μm data are 1.0 ± 0.5 mG, 1.0 ± 0.5 mG, and 2.2 ± 1.2 mG, while those from the 850 μm data are 0.7 ± 0.4 mG, 0.8 ± 0.4 mG, and 1.9 ± 1.1 mG in the 20MC, 50MC, and CNL regions, respectively. The magnetic field strength in the CNL is approximately twice that estimated in the 20MC and 50MC. This higher estimate is mainly attributed to the significantly larger σ_v , which is related to the decomposition process as mentioned in Section 3.2.3. It is important to note that our magnetic field strength estimations, especially in the CNL, may be overestimated due to potential limitations in the spectral decomposition process.

The difference in magnetic field strengths derived from the 450 and 850 μm data is due to the discrepancy in $n(\text{H}_2)$, which is largely influenced by variations in the observed intensity. As discussed in Section 3.2.1, the intensities at 450 and 850 μm

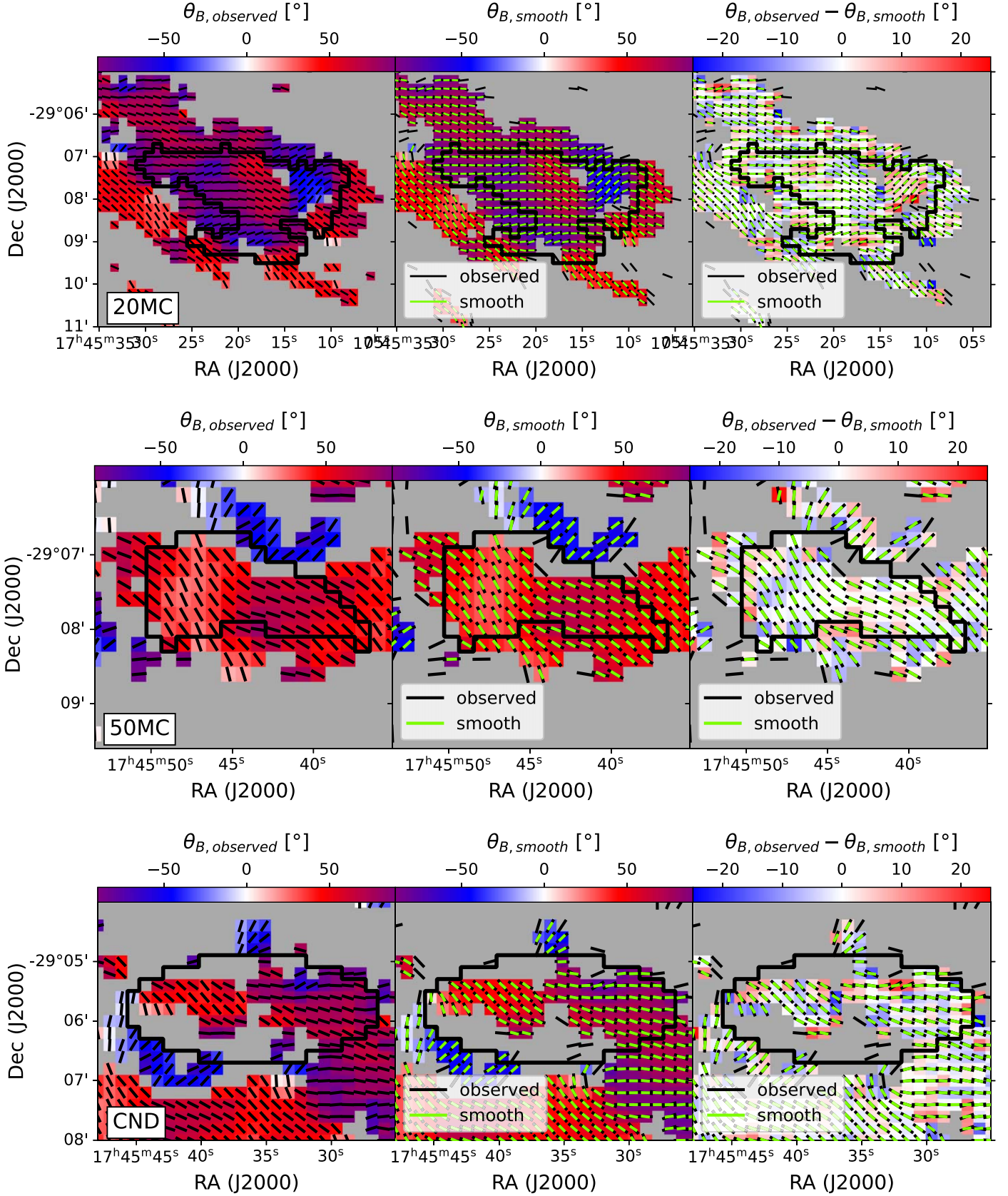


Figure 12. Position angles of magnetic fields θ_B determined by $450\ \mu\text{m}$ polarization in different regions: the 20MC (first row), 50MC (second row), and CND (third row). The position angle ranges from -90° to 90° , with 0° pointing upward. The left panel shows the observed magnetic field position angles $\theta_{B, \text{observed}}$; the central panel shows the mean directions of magnetic field orientations $\theta_{B, \text{smooth}}$; the right panel shows the angle differences by subtracting the smooth position angles from the observed ones using Equation (6), $\theta_{B, \text{observed}} - \theta_{B, \text{smooth}}$. The black segments are the half-vector of $\theta_{B, \text{observed}}$, and the green ones are the half-vector of $\theta_{B, \text{smooth}}$. The black contours show the boundaries of different structures.

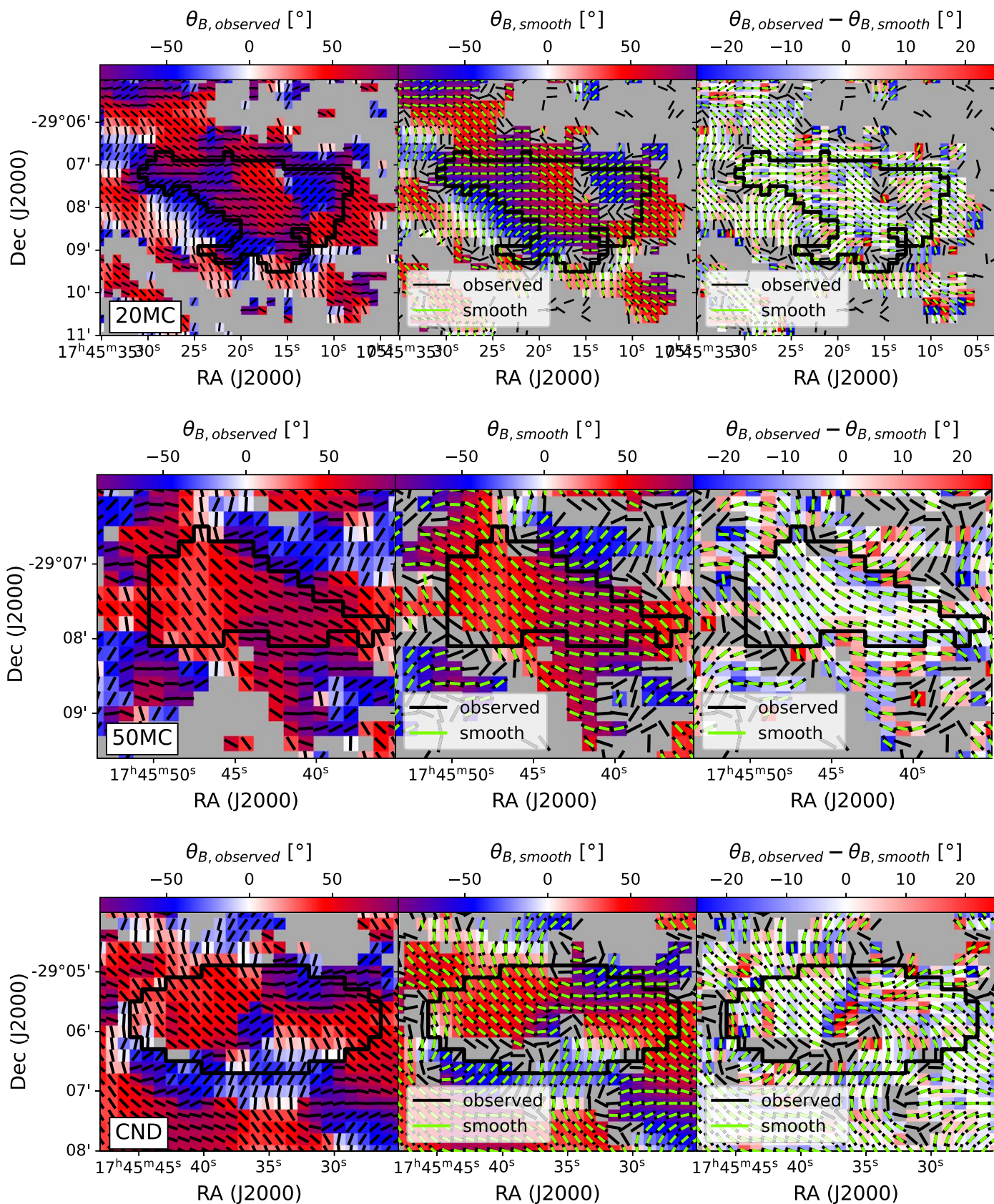


Figure 13. Same as Figure 12 but for the 850 μm data.

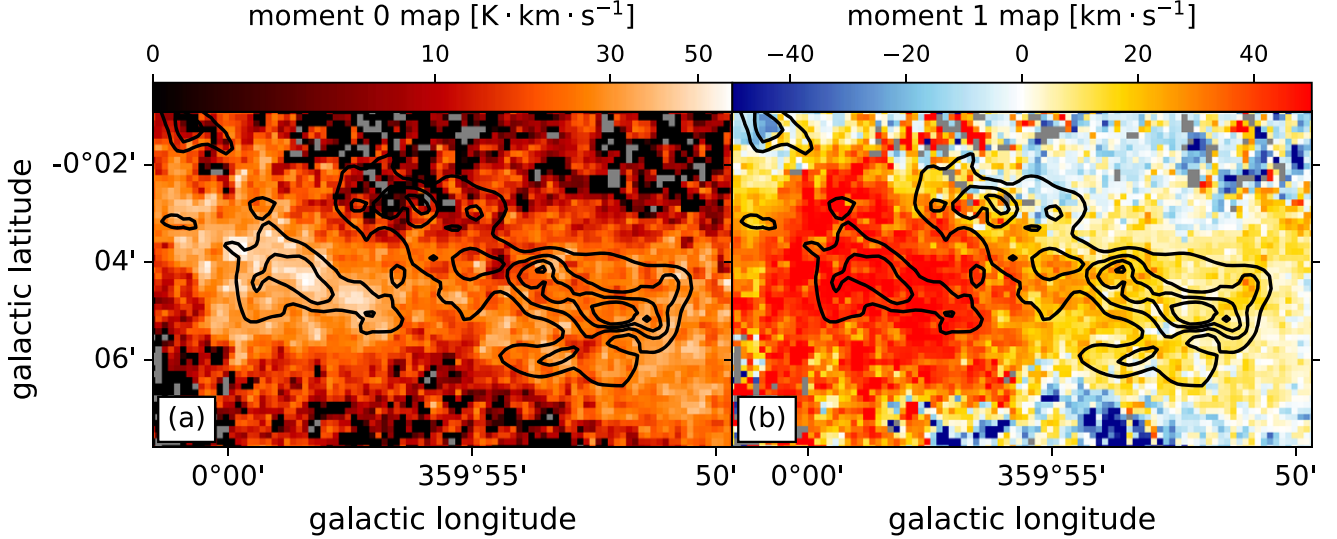


Figure 14. The zeroth and first moment maps of NRO C¹⁸O (1–0) with 15'' resolution shown in panel (a) and panel (b), respectively. The black contours show the 850 μm intensities with the levels of [0.8, 1.6, 2.4, 3.2] Jy beam⁻¹.

are not consistent with a common SED, suggesting that they may not trace the same dust structures along the LOS. This discrepancy is likely due to missing flux issues (see [Appendix](#) for details). Consequently, we interpret the magnetic field strengths derived from different wavelengths as probing slightly different regions along the LOS.

X. Lu et al. (2024) concluded that self-gravity and turbulence play a more dominant role in star formation, based on the weak correlation between magnetic field strength and SFR. However, we believe this weak correlation does not imply star formation is unaffected by magnetic fields; rather, it suggests the SFR is not linearly correlated with magnetic field strength. Star-forming processes should not depend solely on the influence of the magnetic field. Therefore, comparing the energy budgets of the magnetic field, gravity, turbulence, and thermal energy is essential.

3.3. Alfvén Mach Number

The relative importance between the magnetic field and the nonthermal motions can be described by the Alfvén Mach number (M_A), which is a crucial factor in the cloud evolution models. The definition of the Alfvén Mach number is

$$M_A = \sqrt{3} \frac{\sigma_{\text{NT}}}{V_A}, \quad (15)$$

where the Alfvén speed is

$$V_A = \frac{B}{\sqrt{4\pi\rho}}. \quad (16)$$

Here, σ_{NT} represents the nonthermal velocity dispersion, which we assume is due to turbulent perturbation, and V_A is the Alfvén velocity. By incorporating Equations (8), (9), and (16) into Equation (15), we obtain

$$M_A \approx \frac{\sqrt{3} \pi \sigma_\theta}{4 Q}. \quad (17)$$

This formula implies that the Alfvén Mach number can be estimated directly from the angular dispersion of magnetic field orientations.

We estimate the Alfvén Mach number for the 20MC, 50MC, and CND using Equation (17), and present the results in Table 3. The values are within the range of 0.3–0.5, indicating the nonthermal motions are sub-Alfvénic.

3.4. Thermal to Magnetic Energy

To determine the importance of the magnetic field relative to the thermal energy, we adopt the standard β_{plasma} , the gas-to-magnetic pressure ratio, defined by

$$\beta_{\text{plasma}} = \frac{P_{\text{gas}}}{P_{\text{mag}}} = \frac{2c_s^2}{V_A^2}, \quad (18)$$

where

$$c_s = \sqrt{\frac{k_B T}{\mu_{\text{H}_2} m_H}}. \quad (19)$$

Here, P_{gas} is the gas pressure, P_{mag} is the magnetic pressure, and c_s is the sound speed. We consider the dust temperature to calculate the sound speed under the assumption of the gas and dust being in thermal equilibrium. If β_{plasma} is smaller than 1, it implies a magnetically dominated regime.

We calculate β_{plasma} for the 20MC, 50MC, and CND, and the results are presented in Table 3. All β_{plasma} values are much smaller than 1, on the order of $\sim 10^{-4}$, suggesting magnetic field dominance.

3.5. Mass-to-flux Ratio

The significance of magnetic fields in the relation to gravity is crucial when considering gravitational instability, which can be assessed through the mass-to-flux ratio. T. Nakano & T. Nakamura (1978) proposed a critical mass-to-flux ratio, $(M/\Phi)_{\text{crit}} = (2\pi\sqrt{G})^{-1}$, for an isothermal gaseous disk threaded perpendicularly by a uniform, frozen-in magnetic field using linear perturbation analysis. It is common to express the mass-to-flux ratio in the unit of the critical value, which is defined as $\lambda \equiv (M/\Phi)_{\text{obs}} / (M/\Phi)_{\text{crit}}$. The molecular cloud is gravitationally stable when $\lambda < 1$, regarded as “magnetically subcritical.” In contrast, if $\lambda > 1$, named as “magnetically

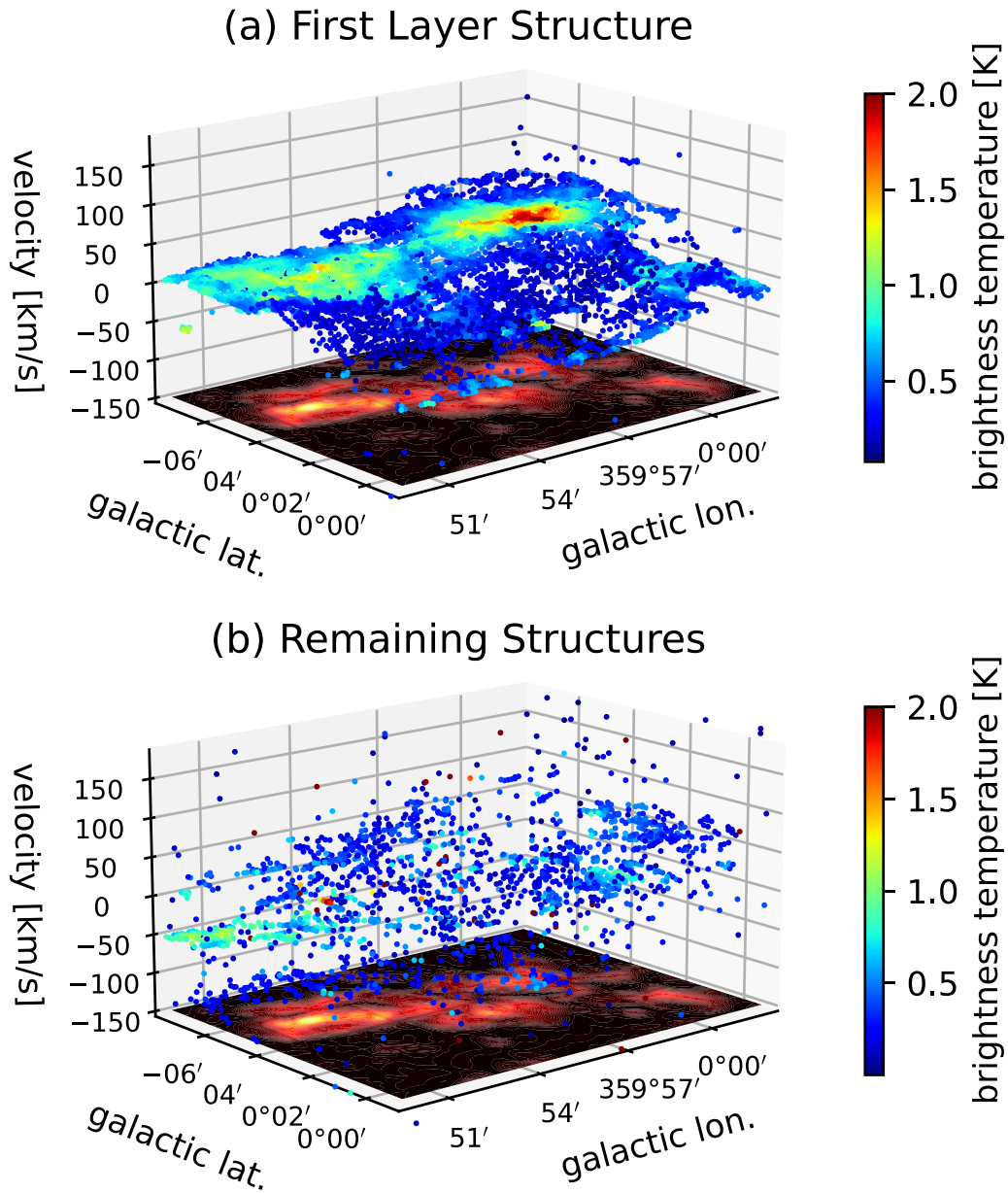


Figure 15. The peak velocities determined from multiple Gaussian fitting using NRO C¹⁸O (1–0) data, shown in PPV space. Panel (a): the first layer structure. Panel (b): The remaining structures, excluding the first layer structure. Data points where the fitting amplitude value is less than 5 times the fitting error are excluded. The surface on the bottom shows the 850 μ m intensity.

supercritical,” the cloud will be unstable and start to collapse toward the center. The mass-to-flux ratio can be determined from observations using the column density N and the magnetic field strength $|B|$:

$$\lambda = \frac{(M/\Phi)_{\text{obs}}}{(M/\Phi)_{\text{crit}}} = \frac{(mNA)/(|B|A)}{(2\pi\sqrt{G})^{-1}} \approx 7.6 \times 10^{-21} \frac{N(\text{H}_2)}{|B|}. \quad (20)$$

Figure 17 displays the relationship between the total magnetic field strength and hydrogen molecule column density. The dashed line represents the critical value for the mass-to-flux ratio. Dots located above the dashed line indicate a subcritical condition, while dots below the line signify a supercritical condition. Based on the estimations, the λ values for the 20MC, 50MC, and CND are subcritical.

R. M. Crutcher (2004) showed that a statistical average mass-to-flux ratio for the strongly magnetized case is

$$\left(\frac{\bar{M}}{\bar{\Phi}}\right) = \int_0^{\pi/2} \frac{M \cos \theta}{\Phi / \sin \theta} \sin \theta \, d\theta = \frac{1}{3} \left(\frac{M}{\Phi}\right)_{\text{obs}}, \quad (21)$$

where clouds have a disklike morphology. We calculate the mass-to-flux ratio using Equation (21) normalized to the critical value using this statistical average and show the results in Table 3. The average mass-to-flux ratios are consistently below 1 within the regions of 20MC, 50MC, and CND, suggesting that these structures are stable and effectively supported by the magnetic field.

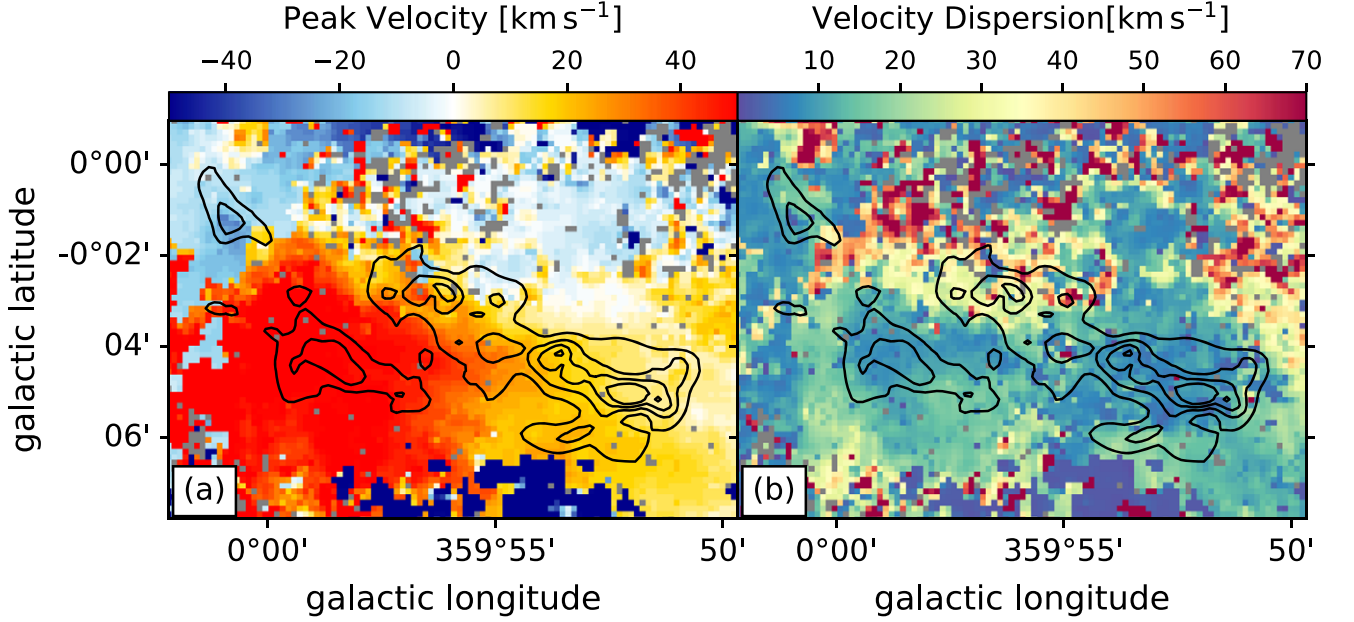


Figure 16. The velocity dispersion determined from $C^{18}O$ (1–0) emission line obtained from NRO. Panel (a): the second moment map. Panel (b): the velocity dispersion map from the first layer structure in the PPV space. Panel (c): the number of the components determined by multiple Gaussian fitting. The contours show the $850 \mu\text{m}$ intensities with the levels of [0.8, 1.6, 2.4, 3.2] Jy beam^{-1} .

Table 3
Magnetic Field Strength and Energy Budget

Region	B_{POS}		B_{tot}		M_{Λ}		$(\tilde{M}/\Phi)/(M/\Phi)_{\text{crit}}$		β_{plasma}	
	(mG)		(mG)						$(\times 10^{-4})$	
	450 μm	850 μm	450 μm	850 μm	450 μm	850 μm	450 μm	850 μm	450 μm	850 μm
20MC	1.0 (0.5)	0.7 (0.4)	1.3 (0.6)	0.9 (0.4)	0.44 (0.02)	0.40 (0.02)	0.18 (0.09)	0.13 (0.07)	1.8 (1.8)	1.7 (1.8)
50MC	1.0 (0.5)	0.8 (0.4)	1.2 (0.6)	1.0 (0.5)	0.32 (0.04)	0.27 (0.03)	0.08 (0.05)	0.05 (0.03)	1.4 (1.4)	1.0 (1.1)
CND	2.2 (1.2)	1.9 (1.1)	2.8 (1.6)	2.5 (1.4)	0.50 (0.04)	0.52 (0.02)	<0.01 (<0.01)	<0.01 (<0.01)	0.8 (0.1)	0.9 (0.1)

Note. Values in parentheses indicate the corresponding uncertainties.

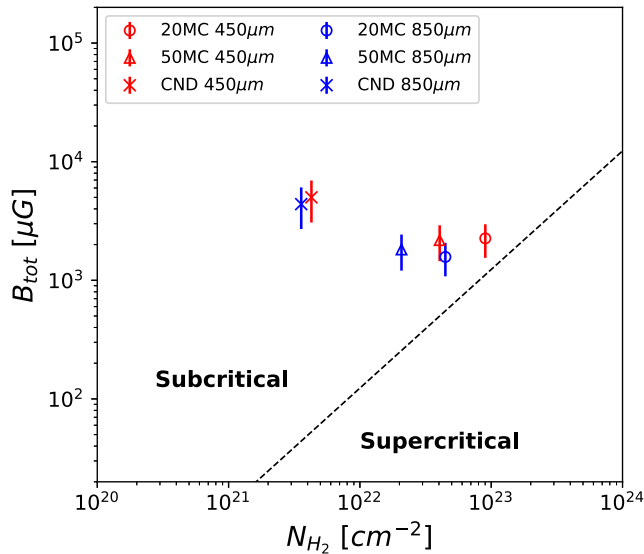


Figure 17. The relation between the total magnetic field strength and the column density of the hydrogen molecule at 450 and 850 μm . The line is for the criterion of $M/\Phi = (M/\Phi)_{\text{crit}}$.

3.6. Grain Alignment Efficiency

The power-law index α of the dependence of the polarization fraction on the total intensity quantifies the grain alignment efficiency, $p \propto I^{-\alpha}$ (B. G. Andersson et al. 2015), assuming that LOS depolarization is negligible. α ranges from 0 to 1. In molecular clouds, the power-law index potentially indicates the alignment efficiency between the dust grains and the magnetic field. If $\alpha \sim 1$, it implies that dust grains are not aligned with any specific direction or are influenced by the disorganized component of the magnetic fields. By contrast, if $\alpha \sim 0$, it indicates that the dust grains are well aligned with each other. Because α may be overestimated due to the non-Gaussian noise characteristics of the polarization fraction, K. Pattle et al. (2019) proposed a ‘‘Ricean-mean model,’’ which can recover α using the mean of the Rice distribution by fitting the p – I relation with the biased polarization fraction p' , as follows:

$$p' = \sqrt{\frac{\pi}{2}} \left(\frac{I}{\sigma_{QU}} \right)^{-1} \mathcal{L}_{\frac{1}{2}} \left[-\frac{p_{\sigma_{QU}}^2}{2} \left(\frac{I}{\sigma_{QU}} \right)^{2(1-\alpha)} \right]. \quad (22)$$

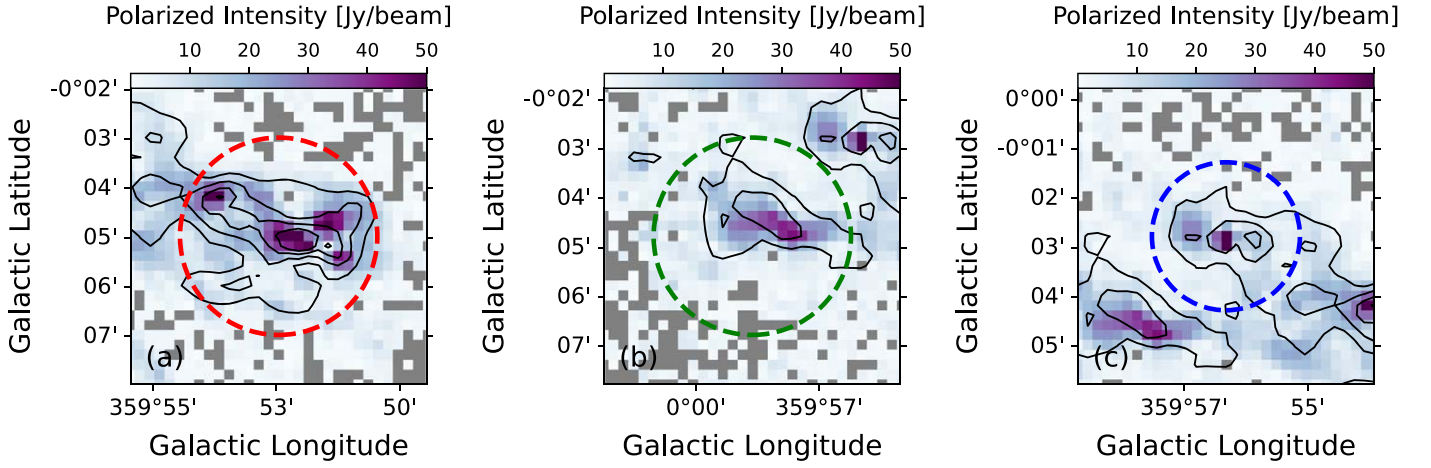


Figure 18. Regions with diameters of $4'$, $4'$, and $3'$ are shown by dashed circles around (a) 20MC, (b) 50MC, and (c) CND, overlaid with the polarization intensity at $850 \mu\text{m}$. The contours show the CO-removed $850 \mu\text{m}$ intensities with the values of $[0.5, 1, 2, 3, 4] \text{ Jy beam}^{-1}$.

Here, σ_{QU} is the average noise in Stokes Q and U from the associated variance V_Q and V_U , $p_{\sigma_{QU}}$ is the polarization fraction at the noise level, and $\mathcal{L}_{\frac{1}{2}}$ is a Laguerre polynomial of order $1/2$. They assume that the observed data can be characterized by a single rms noise value, $\langle\sigma_{QU}\rangle$,

$$\langle\sigma_{QU}\rangle = \frac{1}{2N} \sum_{i=1}^N \sigma_{QU,i} = \frac{1}{2N} \sum_{i=1}^N (\sqrt{V_{Q,i}} + \sqrt{V_{U,i}}). \quad (23)$$

The underlying power-law index, which indicates the alignment efficiency, is revealed when

$$\frac{I}{\sigma_{QU}} > \left(\frac{I}{\sigma_{QU}} \right)_{\text{crit}} = \left(\frac{1}{p_{\sigma_{QU}}} \sqrt{\frac{\pi}{2}} \right)^{\frac{1}{1-\alpha}}. \quad (24)$$

When I/σ_{QU} is lower than the critical value, the power-law index tends to approach -1 . For a detailed verification, see K. Pattle et al. (2019).

To investigate the grain alignment efficiencies in the 20MC, 50MC, and CND, we extract the Stokes I , Q , and U values within circular areas of $4'$ diameter centered on the 20MC and 50MC, and within a $3'$ diameter region centered on the CND, as shown in Figure 18. Using these values, we calculate the biased polarization fractions ($p' = \sqrt{Q^2 + U^2}/I$) and estimate the average noise levels $\langle\sigma_{QU}\rangle$ in each area. We then fit the data points of Stokes I against the biased polarization fraction using the Ricean-mean model. Figure 19 presents the scatter plot of Stokes I versus the biased polarization fraction, with σ_{QU} indicated by different colors. The red solid lines indicate the best-fit Ricean-mean model, the black dashed lines represent the low-SNR limit approximation, $p' = \sqrt{\pi/2} (I/\sigma_{QU})^{-1}$, and the black dotted lines denote the critical value as Equation (24). The data points in Figure 19 are well characterized by $\langle\sigma_{QU}\rangle$ and well fitted by Ricean-mean model.

The fitting results are summarized in Table 4. Except for the polarization observations at $450 \mu\text{m}$ toward the CND, the power-law index α ranges from 0.4 to 0.6, indicating a moderately ordered alignment of the dust grains. In the case of $450 \mu\text{m}$ polarization in the CND region, we obtain a higher power-law index, exceeding 0.79, which implies poor alignment between the magnetic fields and the dust grains.

4. Discussion

4.1. Energy Budget

In Sections 3.3, 3.4, and 3.5, we compared the energy contributions between the magnetic field and the turbulence, kinetic energy, and gravity based on the Alfvén Mach number, β_{plasma} , and mass-to-flux ratio, respectively, within the regions of the 20MC, 50MC, and CND. Our results show these regions are sub-Alfvénic. Furthermore, the β_{plasma} values, all below 1 for the observed structures, indicate the dominance of the magnetic pressure over thermal pressure. Additionally, the mass-to-flux ratios for the 20MC, 50MC, and CND suggest that the magnetic field can effectively counteract gravitational collapse.

The magnetic field strengths of some molecular clouds in the CMZ were measured by previous studies. R. M. Crutcher et al. (1996) obtained the LOS magnetic field strength toward the active star-forming cloud, Sgr B2, as $\sim 0.5 \text{ mG}$ with the VLA using a Zeeman measurement of the H I line. They calculated the β_{plasma} , Alfvén Mach number, and the mass-to-flux ratio as 8×10^{-4} , 0.4, and 2.6, respectively. Their β_{plasma} value is similar to our results, with a value much lower than 1. In Sgr B2, however, their mass-to-flux ratio is higher than 1, indicating that the magnetic field there may not be able to counteract gravitational collapse. This difference could explain why Sgr B2 has a higher SFR compared to the 20MC and 50MC.

In addition, T. Pillai et al. (2015) estimated the total magnetic field strength in G0.253+0.016 as approximately 5 mG using the DCF method and inferred a λ value of roughly 0.6. C. Federrath et al. (2016) adjusted the magnetic field strength to 2.2 mG using an improved average volume density. There, the magnetic field emerges as a dominant factor in this massive molecular cloud, which is similar in environment to the 20MC and 50MC. These moderate values of λ shared by all three clouds may be consistent with the comparatively lower SFRs in G0.253+0.016, the 20MC, and the 50MC.

The material within the CND is influenced by the gravitational potential of a supermassive black hole and follows a quasi-Keplerian rotation, indicating that gravity is dominant. Our results show a subcritical condition for the mass-to-flux ratio in this region, suggesting the magnetic field is more significant. M. S. Akshaya & T. Hoang (2024) produced a pixel-by-pixel mass-to-flux ratio map

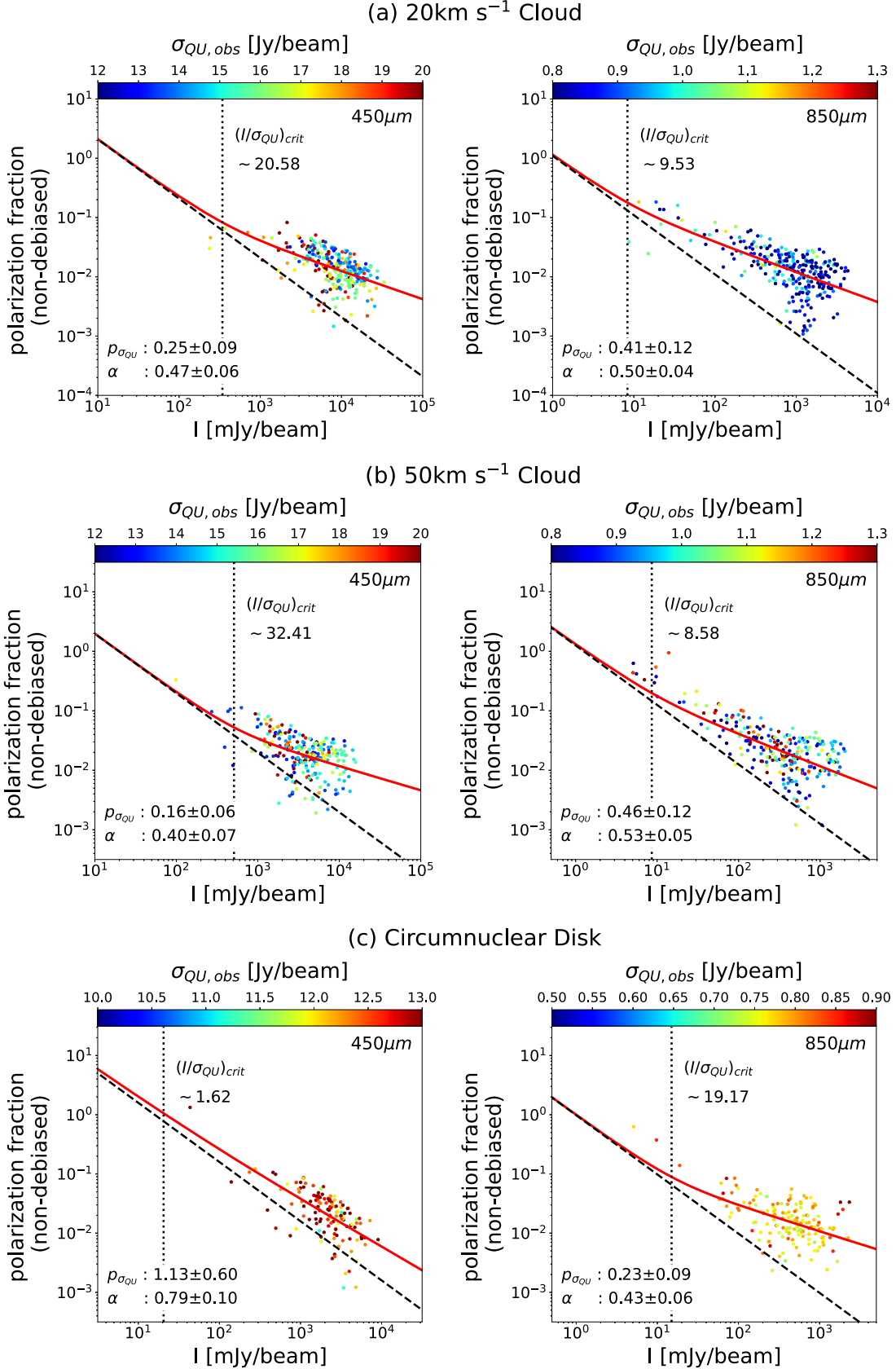


Figure 19. The biased polarization fraction against the Stokes I for (a) 20MC, (b) 50MC, and (c) CND. The data are extracted within the boundaries shown in Figure 18. The red solid lines show the fitting results using Ricean-mean model. The black dashed lines present the low-SNR limit approximation of Equation (22). The black dotted lines indicate the critical value derived from Equation (24).

Table 4
Fitting Results Using Ricean-mean Model for 20MC, 50MC, and CND

Region	$\langle\sigma_{QU}\rangle$	Ricean-mean Model	
		α	$P_{\sigma_{QU}}$
450 μm			
20MC	16.61	0.47 ± 0.06	0.25 ± 0.09
50MC	15.75	0.40 ± 0.07	0.16 ± 0.06
CND	12.69	0.79 ± 0.10	1.13 ± 0.60
850 μm			
20MC	0.88	0.50 ± 0.04	0.41 ± 0.12
50MC	1.00	0.53 ± 0.05	0.46 ± 0.12
CND	0.78	0.43 ± 0.06	0.23 ± 0.09

and found a supercritical condition only within the armlike structures, which are dense regions with low magnetic field strength. Our subcritical result may be due to us estimating an average value within the CND region, which contains both mass-to-flux ratios higher and lower than 1. Additionally, it is also possible the magnetic field strength has been overestimated given the potential limitations in spectral decomposition (see Section 3.2.4).

Consequently, the 20MC, 50MC, and the CND exhibit strong turbulence, as evidenced by their high velocity dispersions, a feature supported by previous studies. Our findings here reveal a significant magnetic field in these regions, as well, suggesting that the magnetic field dominates the overall energy budget.

4.2. Magnetized Field and Density Relation

The magnetic field strengths in self-gravitating clouds can be enhanced through the contraction of collapsing material when the magnetic fields are initially too weak to resist the collapse of the cloud. R. M. Crutcher et al. (2010) analyzed the LOS magnetic field strengths B_{LOS} from Zeeman measurements using a Bayesian approach, and suggested a generalized model to describe the relationship between the cloud density and the maximum magnetic field strength in a cloud, as follows:

$$B_{\text{max}}(n) = \begin{cases} B_0, & n < n_0 \\ B_0 \left(\frac{n}{n_0}\right)^\kappa, & n > n_0 \end{cases} \quad (25)$$

where n is the number density of the hydrogen atom ($n_{\text{H}} = 2n_{\text{H}_2}$). The critical volume density n_0 distinguishes the diffuse interstellar medium and dense molecular clouds. Their results showed $B_0 \approx 10 \mu\text{G}$, $n_{0,\text{H}} \approx 300 \text{ cm}^{-3}$, and $\kappa \approx 0.65$.

Assuming that the magnetic fields traced by the 450 and 850 μm observations correspond to slightly different regions along the LOS, we apply our DCF calculations to explore the relationship between magnetic field strength and density. In Figure 20, we show the relationship between the total magnetic field strength and the volume density of molecular hydrogen based on our calculations, comparing with the expectations from R. M. Crutcher et al. (2010) depicted by a dashed line. We also plot the data for another molecular cloud within the CMZ, G0.253+0.016, obtained from C. Federrath et al. (2016) with DCF method. All data points in Figure 20 are positioned above the dashed line. We fit all data points with Equation (25)

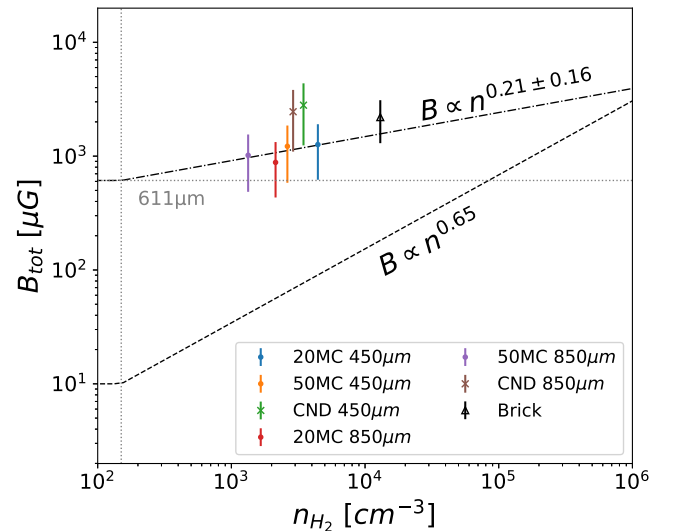


Figure 20. The relation between the total magnetic field strength and the number density of the hydrogen molecule at 450 and 850 μm . The dashed line shows the most probable maximum values for the magnetic field strength by the Bayesian analysis (R. M. Crutcher et al. 2010). We fit power-law index using the data of 20MC, 50MC, and Brick (C. Federrath et al. 2016) and depict the result by dashed-dotted line.

excluding the two points of CND because the CND is a torus-like structure rotating around Sgr A*, as opposed to being a self-gravitating cloud. We obtain the power-law index $\kappa = 0.21 \pm 0.16$ (dashed-dotted line in Figure 20), a value lower than the R. M. Crutcher et al. (2010) result of 0.65. A. Tritsis et al. (2015) demonstrated that the power-law index of the B - n relation could be directly related to the cloud geometry and the respective dominant direction of collapse, assuming a frozen-in magnetic field in the absence of significant ambipolar diffusion. Our result of low κ implies that the contraction motions tend to align with the magnetic field lines without significantly altering the magnetic field strengths. It is important to note, however, that the prescription of the B - n relation is based on spherically collapsing clouds. Such a framework may not be broadly applicable to such a complex and dynamic region as the inner CMZ.

Additionally, the total magnetic field strength B_{tot} is $\sim 611 \mu\text{G}$ at the critical density $n_{0,\text{H}_2} = 150 \text{ cm}^{-3}$, a value roughly 50 times that found in the model by R. M. Crutcher et al. (2010). Note, however, that they used the LOS magnetic field strengths to find the relation. B_{LOS} is roughly half of B_{tot} . This difference implies that the magnetic fields in the molecular clouds in the CMZ environment are typically stronger than those of the closer regions described in R. M. Crutcher et al. (2010).

5. Conclusion

We present the first-look results of the continuum and polarization observations at 450 and 850 μm toward the inner region of the CMZ using SCUBA-2 with the polarimeter POL-2 as part of the BISTRO project. Our investigation focuses on the magnetic field morphology and strength in the inner region of the CMZ, covering three distinct areas: the 20MC, 50MC, and CND. The main findings of this work are as follows:

1. The magnetic field morphology is highly ordered, with the angular dispersion ranging from 5° to 10° . In the

- vicinity of CND, the magnetic field exhibits a spiral structure at both 450 and 850 μm .
2. We derive average POS magnetic field strengths of 1.0 ± 0.5 mG, 1.0 ± 0.5 mG, 2.2 ± 1.2 mG at 450 μm and 0.7 ± 0.4 mG, 0.8 ± 0.4 mG, 1.9 ± 1.1 mG at 850 μm for the 20MC, 50MC, and CND, respectively.
 3. Within the 20MC, 50MC, and CND, magnetic turbulence is sub-Alfvénic, and the magnetic fields are more dominant than thermal pressure. Additionally, the mass-to-flux ratios are all less than 1, indicating the magnetic field can support these structures against gravitational collapse.
 4. Except for the 450 μm polarization in the vicinity of the CND, which is affected by poor observation quality, the power-law indices for the dependence of polarization fraction on total intensity range from 0.4 to 0.6, indicating that dust grains are moderately aligned with the magnetic field in the vicinity of the 20MC, 50MC, and the CND.
 5. Previous studies suggest that the low SFR within the CMZ is possibly due to strong turbulence. Our results, however, reveal the presence of a very strong magnetic field, which may instead be the dominant factor to the energy budgets of these clouds.

Acknowledgments

The James Clerk Maxwell Telescope is operated by the East Asian Observatory on behalf of the National Astronomical Observatory of Japan; Academia Sinica Institute of Astronomy and Astrophysics; the Korea Astronomy and Space Science Institute; the Operation, Maintenance and Upgrading Fund for Astronomical Telescopes and Facility Instruments, funded by the Ministry of Finance (MOF) of China and administrated by the Chinese Academy of Sciences (CAS), as well as the National Key R&D Program of China (No. 2017YFA0402700). Additional funding support is provided by the Science and Technology Facilities Council of the United Kingdom and participating universities in the United Kingdom and Canada. Funding for the construction of SCUBA-2 and POL-2 was provided by the Canada Foundation for Innovation. The Starlink software (H. S. Thomas & M. J. Currie 2014) is supported by the East Asian Observatory, JCMT Project Code M16AL004. This research used the facilities of the Canadian Astronomy Data Centre operated by the National Research Council of Canada with the support of the Canadian Space Agency. This research utilized the NASA Astrophysics Data System. The authors wish to recognize and acknowledge the very significant cultural role and reverence that the summit of Maunakea has always had within the indigenous Hawaiian community. We are privileged to conduct observations from this mountain. We thank the anonymous referee for the thoughtful comments and suggestions, which have helped improve this manuscript. The data used in this paper were obtained under project codes M20AL018, M17AP074. M.Z.Y. and S.P.L. acknowledge grants from the National Science and Technology Council (NSTC) of Taiwan 109-2112-M-007-010-MY3 and 112-2112-M-007-011. This work used high-performance computing facilities operated by the Center for Informatics and Computation in Astronomy (CICA) at National Tsing Hua University. This equipment was funded by the Ministry of Education of Taiwan, the National Science and Technology Council of Taiwan, and National Tsing Hua University. F.P. acknowledges support from the MICINN

under grant No. PID2022-141915NB-C21. M.T. is supported by JSPS KAKENHI grant No. 24H00242. J.K. (Jungmi Kwon) is supported by JSPS KAKENHI grant No. 24K07086. W.K. was supported by the National Research Foundation of Korea (NRF) grant funded by the Korea government (MSIT; RS-2024-00342488). K.P. is a Royal Society University Research Fellow, supported by grant No. URF\R1\211322. X.L. acknowledges support from the National Key R&D Program of China (No. 2022YFA1603101), the Strategic Priority Research Program of the Chinese Academy of Sciences (CAS) grant No. XDB0800300, the National Natural Science Foundation of China (NSFC) through grant Nos. 12273090 and 12322305, the Natural Science Foundation of Shanghai (No. 23ZR1482100), and the CAS ‘‘Light of West China’’ Program No. xbzg-zdsys-202212. J.K. is supported by the Royal Society under grant No. RF\ERE\231132, as part of project URF\R1\211322. K.Q. acknowledges National Natural Science Foundation of China (NSFC) grant Nos. 12425304 and U1731237, and the National Key R&D Program of China with Nos. 2023YFA1608204 and 2022YFA1603103. C.W.L. acknowledges support from the Basic Science Research Program through the NRF funded by the Ministry of Education, Science and Technology (NRF- 2019R1A2C1010851) and from the Korea Astronomy and Space Science Institute grant funded by the Korea government (MSIT; project No. 2024-1-841-00). L.F. acknowledges support from the Ministry of Science and Technology of Taiwan under grant No. 111-2112-M-005-018-MY3. E.S. is supported by the National Natural Science Foundation of China (NSFC), Grant No. 11988101, and by the Alliance of International Science Organizations (ANSO), Grant No. ANSO-VF-2021-01.

Facility: James Clerk Maxwell Telescoping (JCMT).

Software: Starlink (M. J. Currie et al. 2014), astropy (Astropy Collaboration et al. 2013, 2018, 2022).

Appendix

CO Contamination Removal and Missing Flux Issue

We attempt to remove the CO emission using the JCMT CHIMPS2 observations from the BISTRO continuum observations during the SCUBA-2 data reduction following the method outlined by T. J. T. Moore et al. (2015). They treated the CO map as a negative fake source and incorporated it into the reduction pipeline. Our results, however, suggest that the CHIMPS2 observations are not appropriate for incorporation into our intensity map due to the differences in the scales of the structures traced.

First, we calculate the zeroth moment map using the ^{12}CO (3–2) observations and convert the units from a brightness temperature to pW, the SCUBA-2 output power units, using the parameters in T. J. T. Moore et al. (2015). The details are as follows: (1) the zeroth moment map is divided by the forward spillover and scattering efficiency $\eta_{\text{fss}} = 0.71$, (2) it is multiplied by the conversion factor $C = 0.77$ (from effective brightness temperature to mJy beam $^{-1}$), and (3) the FCF value of 516 (from mJy beam $^{-1}$ to pW) is applied along with the POL-2 transmission factor of 1.35. We show the BISTRO 850 μm intensity map and ^{12}CO (3–2) intensity map with the unit of pW in panels (a) and (b) of Figure 21. In panel (a), the brightest dust emission at 850 μm is observed in the 20MC. In contrast, the brightest ^{12}CO (3–2) emission is found near the CND, as shown in panel (b).

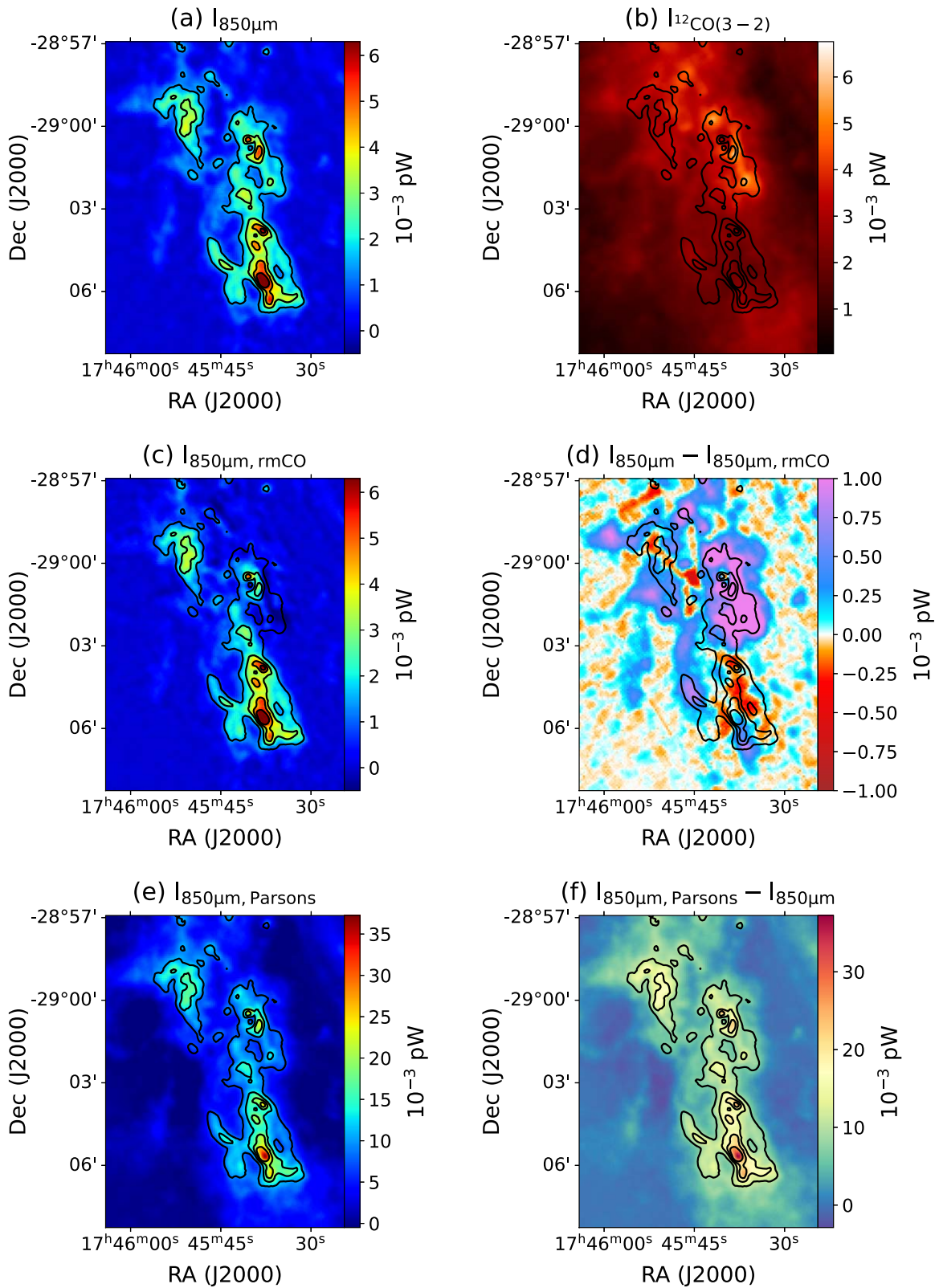


Figure 21. Results of CO contamination removal during the map-making data reduction process. Panel (a): original continuum intensity at 850 μm observed by SCUBA-2 equipped with POL-2. Panel (b): ^{12}CO (3–2) intensity. Panel (c): the intensity at 850 μm with CO contamination removal during the map-making process using the gas intensity shown in panel (b). Panel (d): the gas intensity eliminated from the continuum observations at 850 μm . Panel (e): the intensity at 850 μm from H. Parsons et al. (2018) observed by SCUBA-2. Panel (f): difference between the intensity maps from this work and that of H. Parsons et al. (2018).

Subsequently, we treat the CO intensity map as the fake source map applied to the map-making process. The resulting dust intensity map with CO contamination removed is shown in panel (c) of Figure 21. Then, we subtract the CO-removed intensity from the original data and display the result in panel (d). Unexpectedly, the CO-removed intensity map has larger values than the original maps of the 20MC and 50MC. We suspect this issue is due to the problem of flux missing from the extended structures.

H. Parsons et al. (2018) produced a CO contamination map using the intensity observations taken by SCUBA-2 without POL-2, in combination with CHIMPS2 ^{12}CO (3–2) data. We compare the 850 μm intensity observations from H. Parsons et al. (2018) to our data. The difference is shown in panel (f) of Figure 21. This map shows that the intensity map from H. Parsons et al. (2018) captures the larger structure. The discrepancy is likely due to the different SCUBA-2 observing modes: “DAISY” and “PONG.” The observing mode used in our BISTRO data is DAISY, which is designed for small, compact sources of around $3'$ or less. In contrast, H. Parsons et al. (2018) utilized the PONG mode, another scan strategy intended for covering large areas (for a detailed introduction of two observing modes, see H. S. Thomas & M. J. Currie 2014). Additionally, the CHIMPS2 observations were taken with HARP on JCMT, designed to rapidly scan large regions. The PONG intensity map and the gas emission map obtained with HARP trace structures on similar scales, enabling H. Parsons et al. (2018) to produce a reliable map of CO contamination levels. In our case, however, the CHIMPS2 observations are not suitable for incorporation into our DAISY intensity map for CO contamination removal.

For results, we adopt the CO contamination fraction derived by H. Parsons et al. (2018) rather than eliminate CO emission during the reduction process, as shown in Figure 4. The ^{12}CO (3–2) contamination ranges from 0% to 30% in the vicinity of the 20MC and 50MC, and reaches up to $\sim 80\%$ in the CN region. Under the assumption of local thermodynamic equilibrium, the ^{12}CO (6–5) contamination is nearly zero in the 20MC and 50MC, but still exceeds $\sim 80\%$ in the CN region.

ORCID iDs

Meng-Zhe Yang  <https://orcid.org/0009-0003-5699-2723>
 Shih-Ping Lai  <https://orcid.org/0000-0001-5522-486X>
 Janik Karoly  <https://orcid.org/0000-0001-5996-3600>
 Kate Pattle  <https://orcid.org/0000-0002-8557-3582>
 Xing Lu (吕行)  <https://orcid.org/0000-0003-2619-9305>
 David Eden  <https://orcid.org/0000-0002-5881-3229>
 Sheng-Jun Lin  <https://orcid.org/0000-0002-6868-4483>
 Frédérick Poidevin  <https://orcid.org/0000-0002-5391-5568>
 Ekta Sharma  <https://orcid.org/0000-0002-4541-0607>
 Jihye Hwang  <https://orcid.org/0000-0001-7866-2686>
 Lapo Fanciullo  <https://orcid.org/0000-0001-9930-9240>
 Mehrnoosh Tahani  <https://orcid.org/0000-0001-8749-1436>
 Patrick M. Koch  <https://orcid.org/0000-0003-2777-5861>
 Shu-ichiro Inutsuka  <https://orcid.org/0000-0003-4366-6518>
 Valentin J. M. Le Gouellec  <https://orcid.org/0000-0002-5714-799X>
 Hao-Yuan Duan  <https://orcid.org/0000-0002-7022-4742>
 Jia-Wei Wang  <https://orcid.org/0000-0002-6668-974X>
 Gary Fuller  <https://orcid.org/0000-0001-8509-1818>
 Ray S. Furuya  <https://orcid.org/0000-0003-0646-8782>
 Qilao Gu  <https://orcid.org/0000-0002-2826-1902>
 Tetsuo Hasegawa (長谷川哲夫)  <https://orcid.org/0000-0003-1853-0184>

Guangxing Li  <https://orcid.org/0000-0003-3144-1952>
 Junhao Liu (劉峻豪)  <https://orcid.org/0000-0002-4774-2998>
 M. S. Akshaya  <https://orcid.org/0000-0001-6258-7474>
 Bijas Najimudeen  <https://orcid.org/0000-0002-6398-7530>
 Le Ngoc Tram  <https://orcid.org/0000-0002-6488-8227>
 Derek Ward-Thompson  <https://orcid.org/0000-0003-1140-2761>
 Doris Arzoumanian  <https://orcid.org/0000-0002-1959-7201>
 James Di Francesco  <https://orcid.org/0000-0002-9289-2450>
 Yasuo Doi  <https://orcid.org/0000-0001-8746-6548>
 Thiem Hoang  <https://orcid.org/0000-0003-2017-0982>
 Ji-hyun Kang  <https://orcid.org/0000-0001-7379-6263>
 Jungmi Kwon  <https://orcid.org/0000-0003-2815-7774>
 Woojin Kwon  <https://orcid.org/0000-0003-4022-4132>
 Chang Won Lee (이창원)  <https://orcid.org/0000-0002-3179-6334>
 Tie Liu (劉鐵)  <https://orcid.org/0000-0002-5286-2564>
 Takashi Onaka  <https://orcid.org/0000-0002-8234-6747>
 Sarah Sadavoy  <https://orcid.org/0000-0001-7474-6874>
 Motohide Tamura  <https://orcid.org/0000-0002-6510-0681>
 Pierre Bastien  <https://orcid.org/0000-0002-0794-3859>
 David Berry  <https://orcid.org/0000-0001-6524-2447>
 Simon Coudé  <https://orcid.org/0000-0002-0859-0805>
 Keping Qiu  <https://orcid.org/0000-0002-5093-5088>

References

- Akshaya, M. S., & Hoang, T. 2024, *MNRAS*, 531, 5012
 Andersson, B. G., Lazarian, A., & Vaillancourt, J. E. 2015, *ARA&A*, 53, 501
 Astropy Collaboration, Price-Whelan, A. M., Lim, P. L., et al. 2022, *ApJ*, 935, 167
 Astropy Collaboration, Price-Whelan, A. M., Sipőcz, B. M., et al. 2018, *AJ*, 156, 123
 Astropy Collaboration, Robitaille, T. P., Tollerud, E. J., et al. 2013, *A&A*, 558, A33
 Bastien, P., Bissonnette, E., Simon, A., et al. 2011, in ASP Conf. Ser. 449, *Astronomical Polarimetry 2008: Science from Small to Large Telescopes*, ed. P. Bastien et al. (San Francisco, CA: ASP), 68
 Berry, D. S., Gledhill, T. M., Greaves, J. S., & Jenness, T. 2005, in ASP Conf. Ser. 343, *Astronomical Polarimetry: Current Status and Future Directions*, ed. A. Adamson et al. (San Francisco, CA: ASP), 71
 Chandrasekhar, S., & Fermi, E. 1953, *ApJ*, 118, 113
 Chapin, E. L., Berry, D. S., Gibb, A. G., et al. 2013, *MNRAS*, 430, 2545
 Crutcher, R. M. 1999, *ApJ*, 520, 706
 Crutcher, R. M. 2004, in *The Magnetized Interstellar Medium*, ed. B. Uyaniker, W. Reich, & R. Wielebinski (Katlenburg-Lindau: Copernicus GmbH), 123
 Crutcher, R. M., Roberts, D. A., Mehringer, D. M., & Troland, T. H. 1996, *ApJL*, 462, L79
 Crutcher, R. M., Wandelt, B., Heiles, C., Falgarone, E., & Troland, T. H. 2010, *ApJ*, 725, 466
 Currie, M. J., Berry, D. S., Jenness, T., et al. 2014, in ASP Conf. Ser. 485, *Astronomical Data Analysis Software and Systems XXIII*, ed. N. Manset & P. Forshay (San Francisco, CA: ASP), 391
 Davis, L. 1951, *PhRv*, 81, 890
 Davis, L., Jr., & Greenstein, J. L. 1951, *ApJ*, 114, 206
 Dempsey, J. T., Friberg, P., Jenness, T., et al. 2013, *MNRAS*, 430, 2534
 Drabek, E., Hatchell, J., Friberg, P., et al. 2012, *MNRAS*, 426, 23
 Draine, B. T., & Weingartner, J. C. 1996, *ApJ*, 470, 551
 Eden, D. J., Moore, T. J. T., Currie, M. J., et al. 2020, *MNRAS*, 498, 5936
 Federrath, C., Rathborne, J. M., Longmore, S. N., et al. 2016, *ApJ*, 832, 143
 Ferrière, K., Gillard, W., & Jean, P. 2007, *A&A*, 467, 611
 Friberg, P., Bastien, P., Berry, D., et al. 2016, *Proc. SPIE*, 9914, 991403
 Ginsburg, A., Bally, J., Barnes, A., et al. 2018, *ApJ*, 853, 171
 Hildebrand, R. H., Davidson, J. A., Dotson, J., et al. 1993, *ApJ*, 417, 565
 Hildebrand, R. H., Gonatas, D. P., Platt, S. R., et al. 1990, *ApJ*, 362, 114
 Holland, W. S., Bintley, D., Chapin, E. L., et al. 2013, *MNRAS*, 430, 2513
 Hsieh, P.-Y., Koch, P. M., Kim, W.-T., et al. 2018, *ApJ*, 862, 150
 Hsieh, P.-Y., Koch, P. M., Kim, W.-T., et al. 2019, *ApJL*, 885, L20
 Hsieh, P.-Y., Koch, P. M., Kim, W.-T., et al. 2021, *ApJ*, 913, 94
 Hu, Y., Lazarian, A., & Wang, Q. D. 2022, *MNRAS*, 511, 829

- Hwang, J., Kim, J., Pattle, K., et al. 2021, *ApJ*, 913, 85
- Karoly, J., Ward-Thompson, D., Pattle, K., et al. 2025, *ApJL*, 982, L22
- Kennicutt, R. C., Jr. 1998, *ApJ*, 498, 541
- Kennicutt, R. C., Jr., & Evans, N. J. 2012, *ARA&A*, 50, 531
- Kirk, J. M., Ward-Thompson, D., Palmeirim, P., et al. 2013, *MNRAS*, 432, 1424
- Koch, P. M., Tang, Y.-W., & Ho, P. T. P. 2012, *ApJ*, 747, 79
- Kruijssen, J. M. D., Dale, J. E., & Longmore, S. N. 2015, *MNRAS*, 447, 1059
- Kruijssen, J. M. D., Longmore, S. N., Elmegreen, B. G., et al. 2014, *MNRAS*, 440, 3370
- Kwon, J., Doi, Y., Tamura, M., et al. 2018, *ApJ*, 859, 4
- Latvakoski, H. M., Stacey, G. J., Gull, G. E., & Hayward, T. L. 1999, *ApJ*, 511, 761
- Lazarian, A., & Hoang, T. 2007, *ApJL*, 669, L77
- Liu, J., Qiu, K., Berry, D., et al. 2019, *ApJ*, 877, 43
- Liu, J., Qiu, K., & Zhang, Q. 2022, *ApJ*, 925, 30
- Longmore, S. N., Bally, J., Testi, L., et al. 2013, *MNRAS*, 429, 987
- Lu, X., Liu, J., Pillai, T., et al. 2024, *ApJ*, 962, 39
- Lu, X., Zhang, Q., Kauffmann, J., et al. 2017a, in IAU Symp. 322, The Multi-Messenger Astrophysics of the Galactic Centre (Cambridge: Cambridge Univ. Press), 99
- Lu, X., Zhang, Q., Kauffmann, J., et al. 2017b, *ApJ*, 839, 1
- Lu, X., Zhang, Q., Kauffmann, J., et al. 2019, *ApJ*, 872, 171
- Mairs, S., Dempsey, J. T., Bell, G. S., et al. 2021, *AJ*, 162, 191
- Mangilli, A., Aumont, J., Bernard, J. P., et al. 2019, *A&A*, 630, A74
- Marsh, K. A., Whitworth, A. P., Lomax, O., et al. 2017, *MNRAS*, 471, 2730
- Mestel, L. 1985, in Protostars and Planets II, ed. D. C. Black & M. S. Matthews (Tucson, AZ: Univ. Arizona Press), 320
- Mills, E., Morris, M. R., Lang, C. C., et al. 2011, *ApJ*, 735, 84
- Minamidani, T., Nishimura, A., Miyamoto, Y., et al. 2016, *Proc. SPIE*, 9914, 99141Z
- Molinari, S., Bally, J., Noriega-Crespo, A., et al. 2011, *ApJL*, 735, L33
- Molinari, S., Schisano, E., Elia, D., et al. 2016, *A&A*, 591, A149
- Moore, T. J. T., Plume, R., Thompson, M. A., et al. 2015, *MNRAS*, 453, 4264
- Morris, M., & Serabyn, E. 1996, *ARA&A*, 34, 645
- Morris, M., & Yusef-Zadeh, F. 1989, *NuPhS*, 10, 59
- Mouschovias, T. C., & Paleologou, E. V. 1986, *ApJ*, 308, 781
- Nakamura, F., & Li, Z.-Y. 2008, *ApJ*, 687, 354
- Nakano, T., & Nakamura, T. 1978, *PASJ*, 30, 671
- Ossenkopf, V., & Henning, T. 1994, *A&A*, 291, 943
- Par , D., Butterfield, N. O., Chuss, D. T., et al. 2024, *ApJ*, 969, 150
- Parsons, H. 2017, The Dusty Galactic Centre as Seen by SCUBA-2, doi:10.11570/17.0009
- Parsons, H., Dempsey, J. T., Thomas, H. S., et al. 2018, *ApJS*, 234, 22
- Pattle, K., Lai, S.-P., Hasegawa, T., et al. 2019, *ApJ*, 880, 27
- Pattle, K., Ward-Thompson, D., Berry, D., et al. 2017, *ApJ*, 846, 122
- Pilbratt, G. L., Riedinger, J. R., Passvogel, T., et al. 2010, *A&A*, 518, L1
- Pillai, T., Kauffmann, J., Tan, J. C., et al. 2015, *ApJ*, 799, 74
- Planck Collaboration, Adam, R., Ade, P. A. R., et al. 2016, *A&A*, 586, A135
- Plante, R. L., Lo, K. Y., & Crutcher, R. M. 1995, *ApJL*, 445, L113
- Reid, M. J., Menten, K. M., Brunthaler, A., et al. 2014, *ApJ*, 783, 130
- Sato, K., Shinnaga, H., Furuya, R. S., et al. 2024, *PASJ*, 76, 960
- Schmidt, M. 1959, *ApJ*, 129, 243
- Soam, A., Pattle, K., Ward-Thompson, D., et al. 2018, *ApJ*, 861, 65
- Thomas, H. S., & Currie, M. J. 2014, *StarC*, 21
- Tokuyama, S., Oka, T., Takekawa, S., et al. 2019, *PASJ*, 71, S19
- Tritsis, A., Panopoulou, G. V., Mouschovias, T. C., Tassis, K., & Pavlidou, V. 2015, *MNRAS*, 451, 4384
- Tsuboi, M., Kitamura, Y., Uehara, K., et al. 2018, *PASJ*, 70, 85
- Tsuboi, M., & Miyazaki, A. 2012, *PASJ*, 64, 111
- Tsuboi, M., Miyazaki, A., & Uehara, K. 2015, in ASP Conf. Ser. 499, Revolution in Astronomy with ALMA: The Third Year, ed. D. Iono et al. (San Francisco, CA: ASP), 249
- Uehara, K., Tsuboi, M., Kitamura, Y., Miyawaki, R., & Miyazaki, A. 2019, *ApJ*, 872, 121
- Wang, J.-W., Lai, S.-P., Eswarajah, C., et al. 2019, *ApJ*, 876, 42
- Ward-Thompson, D., Pattle, K., Bastien, P., et al. 2017, *ApJ*, 842, 66
- Ward-Thompson, D., Pattle, K., Kirk, J. M., et al. 2016, *MNRAS*, 463, 1008
- Wardle, J. F. C., & Kronberg, P. P. 1974, *ApJ*, 194, 249
- Wardle, M., & Konigl, A. 1990, *ApJ*, 362, 120
- Whittet, D. C. B., Hough, J. H., Lazarian, A., & Hoang, T. 2008, *ApJ*, 674, 304
- Yusef-Zadeh, F., Lacy, J. H., Wardle, M., et al. 2010, *ApJ*, 725, 1429